CORA Cork Open Research Archive
Cartlann Taighde Oscailte Chorcaí

Title	Investigation of barge-type FOWT in the context of concurrent and cascading failures within the mooring systems
Authors	Jia, Wenzhe;Liu, Qingsong;Iglesias, Gregorio;Miao, Weipao;Yue, Minnan;Yang, Yang;Li, Chun
Publication date	2024-02-19
Original Citation	Jia, W., Liu, Q., Iglesias, G., Miao, W., Yue, M., Yang, Y. and Li, C. (2024) 'Investigation of barge-type FOWT in the context of concurrent and cascading failures within the mooring systems', Renewable Energy, 224, p.120119 (23pp). https://doi.org/10.1016/j.renene.2024.120119
Type of publication	Article (peer-reviewed)
Link to publisher's version	10.1016/j.renene.2024.120119
Rights	© 2024, Elsevier Ltd. All rights reserved. This manuscript version is made available under the CC BY-NC-ND 4.0 license. - https://creativecommons.org/licenses/by-nc-nd/4.0/
Download date	2026-10-31 07:01:21
Item downloaded from	https://hdl.handle.net/10468/16434



UCC
University College Cork, Ireland
Coláiste na hOllscoile Corcaigh

Investigation of Barge-type FOWT in the context of concurrent and cascading failures within the mooring systems

Wenzhe Jia[a], Qingsong Liu[b], Gregorio lglesias[d, e], Weipao Miao[a], Minnan Yue[a], Yang Yang[c], Chun Li[a]

[a] *School of Energy and Power Engineering, University of Shanghai for Science and Technology, Shanghai, 200093, P.R.China*

[b] *Liverpool Logistics, Offshore and Marine (LOOM) Research Institute, Liverpool John Moores University, Liverpool, Byrom Street, L3 3AF, United Kingdom.*

[c] *Faculty of Maritime and Transportation, Ningbo University, Ningbo 315211, P.R. China*

[d] *School of Engineering, Computing and Mathematics (SECaM), University of Plymouth, Plymouth, PL 48AA.United Kingdom.*

[e] *School of Engineering and Architecture. University College Cork, lreland. T12 K8AF. UK*

Abstract:

The design requirements for offshore engineering stipulate that floating structures should maintain their overall performance even in the event of a single mooring line failure. However, it is crucial to ensure that the platform does not drift or capsize in the case of two mooring line failures. Therefore, the investigation into the dynamic response of wind turbines after mooring line failures is of great significance. In this study, the aerodynamic-structural simulation capability of FAST was coupled with the hydrodynamic analysis software AQWA by modifying the dynamic link library. The dynamic response of a Barge-type floating offshore wind turbine (FOWT) and the variations in mooring line tensions were computed under different sea conditions after the successive failures of two mooring lines with varying time intervals. The findings reveal that in rated sea conditions, there is a significant increase in surge motion, reaching a maximum value 2.08 times that of the original, following the failure of two mooring lines. The tension in mooring line #3 reaches 1.57 times the pre-failure value. In extreme sea conditions, the simultaneous failure of two mooring lines at the same corner triggers a cascading failure phenomenon within the mooring system, and a shorter interval between failures amplifies the dynamic response of the platform. Therefore, it is not advisable to deploy the Barge platform in harsh environmental conditions.

Keywords: Floating offshore wind turbine, Mooring line failure, Aerodynamic-structural simulation, Hydrodynamic analysis.

Roman symbols

EA	axial stiffness of the mooring	[N/m]
EI	bending stiffness of the mooring	[N/m]
f	wave frequency	[Hz]
F_{AQWA}	the translational force vectors in AQWA	[kN]
F_{FAST}	the translational force vectors in FAST	[kN]
F_h	external hydrodynamic load applied to of the mooring	[kN]
F(t)	total external force vector	[kN]
H_s	significant wave height	[m]
L_k	turbulence integral scale parameter of the velocity component	[m/s]
m_e	mass of per unit length of the mooring	[kg]
M	bending moment vector at the first node of the element	[kN·m]
M_{AQWA}	moment vector acting at the platform's mass center	[kN·m]
M_{FAST}	moment vector acting at the tower-base	[kN·m]
P_B	minimum rated breaking load of the mooring	[kN]
q	distributed moment load per unit length of the mooring	[kN·m]
R	position vector of the first node	[m]
S_e	arbitrary element of the mooring line	[-]

S_k	one-sided spectrum of the velocity component	[m/s]
T	tension force vector at the first node of the mooring	[kN]
T_{max}	maximum tension in the mooring	[kN]
T_z	zero-crossing period	[s]
U_{hub}	the wind speed at the hub	[m/s]
V	shear force vector at the first node of the element	[kN·m]
w	gravity vector per unit length of the element	[kN]
$\mathbf{X}(t)$	displacement vectors of the platform	[m]
$\dot{\mathbf{X}}(t)$	velocity vectors of the platform	[m/s]
$\ddot{\mathbf{X}}(t)$	acceleration vectors of the platform	[m/s^2]

Greek symbols

σ_k	standard deviation of the velocity component	[m/s]
$\boldsymbol{\varepsilon}$	axial strain of the mooring line	[-]
θ_1	roll angles of the platform	[°]
θ_2	pitch angles of the platform	[°]
θ_3	yaw angles of the platform	[°]
ω	wave phase	[°]

1. Introduction

The theme of low-carbon and environmental preservation stands as a prevailing trajectory for global future development, with the wind power industry assuming a pivotal role in attaining sustainable and eco-friendly energy provision [1]. The "Global Wind Report 2022" by the Global Wind Energy Council attests to the rapid expansion of the wind power market, with a staggering new installed capacity of 93.6 GW and an accumulated installed capacity of 837 GW [2]. It is worth highlighting that around 80% of the world's exploitable wind resources lie within the depths of our seas [3], underscoring the immense potential held by FOWT in the forthcoming era. Given their integral status within FOWTs, in-depth examination of their mooring systems assumes paramount significance [4].

FOWTs currently employ three prevalent mooring configurations utilized in the offshore oil and gas sector: tension leg systems, catenary mooring systems, and hybrid mooring systems [5]. The catenary mooring system mainly employs steel chains, which hang in a catenary curve between the floating structure and its anchor. The relaxed catenary of the system leads to flexible vertical and horizontal motion of the floating platform. Tension-leg mooring systems feature mooring lines that are pre-tensioned, ensuring them to be fully tautened by the floating body. Hybrid mooring systems combines the characteristics of both taut and and catenary configurations [6]. Among these, catenary mooring systems rely on the gravitational force exerted by steel chains to constrain platform movement, with the lower portion of the chains resting on the seabed, maintaining a certain degree of catenary length [7]. When the water depth exceeds 150 m, the catenary mooring system emerges as the preferred choice [8]. Extensive research has demonstrated the profound influence of the mooring system's dynamic characteristics on mooring tension [9], platform damping [10], as well as the fatigue and extreme loads endured by the wind turbine [11]. Consequently, accurate modeling of the mooring system stands as a paramount necessity within the design process.

The methodologies for analyzing mooring systems can be categorized into quasi-static and

dynamic analyses [12]. To integrate the dynamic behaviors of both mooring and wind turbine within an analytical framework, Masciola et al.[13][14] employed a fusion of FAST with OrcaFlex to compute mooring dynamics. Their investigation illuminated that the utilization of quasi-static mooring models tends to underestimate the apex mooring loads. During the advancement of FAST v8.16, Wendt et al. [15] embraced a multi-segment quasi-static (MSQS) mooring model. They assessed the mooring system by contemplating the mean loads of catenary and taut mooring configurations. Nonetheless, the quasi-static analytical approach, which computes wave-induced dynamic loads through accounting for static offsets, proves unsuitable for the transient motion analysis of compromised moorings. Jonkman et al. [16] interconnected dynamic mooring systems with the aeroelastic wind turbine code FAST and identified numerical instability while calculating slack catenary line moorings. In a multi-body simulation (MBS) study, Matha et al. [17], in synergy with the commercial multi-body model SIMPACK [18], simulated FOWTs and discerned reduced amplitudes from nonlinear methodologies. The Spanish National Renewable Energy Center (CENER) devised the Offshore Platform Anchorage System Simulator (OPASS) [19], meticulously crafted to emulate nonlinear mooring dynamics. Robertson et al. [20] merged OPASS with NREL's developed FAST program and achieved profoundly satisfactory outcomes. Yang et al. [21] integrated FAST with AQWA's comprehensive computational capabilities, encompassing nonlinear hydrodynamics, mooring dynamics, and material nonlinearity. This integrated approach allowed for a comprehensive dynamic analysis of a FOWT. Following this, a comparative investigation was undertaken, unveiling a remarkable congruence in the dynamic attributes of the platform and the mooring system, both in terms of trend evolution and amplitude fluctuations.

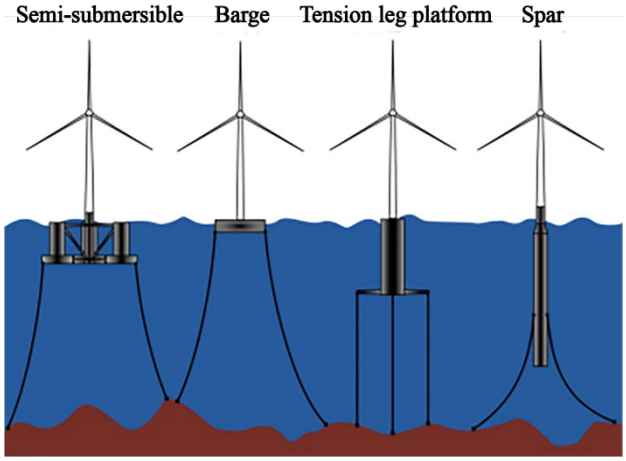


Fig.1 Comparative overview of the four principal FOWT configurations: (L-R) Semi-submersible, Barge, Tension leg platform and Spar

The design and production of offshore wind turbines have benefited from technological advancements in the offshore oil and gas industry. Similarly, the classification of floating platforms draws upon the definitions used for deepwater oil and gas platforms [22]. Floating platforms can be categorized into four types based on their stability mechanisms: Barge platforms, Semi-submersible platforms, Tension Leg Platforms (TLPs), and Spar platforms [23]. The distinctions among various floating structure concepts are illustrated in Fig. 1. Recognizing the critical role of the mooring system for floating platforms, numerous researchers have conducted extensive studies on mooring failures. Li et al. [24] developed a time-domain coupled dynamic model to investigate the transient response of wind turbines on Spar platforms following sudden mooring failure. Their research uncovered significant transient responses of wind turbines when mooring failures occurred. Wu et

al. [25] utilized FAST to examine the transient dynamic response of the WindStar TLP wind turbine in the event of a single mooring line failure. They discovered that when the mooring failure was not aligned with the wave direction, the lateral motion of the wind turbine and nacelle acceleration exhibited significant increases. However, it is important to consider that the blades and tower, being slender structures, may introduce their own oscillations, thereby influencing the environmental loads and dynamic response of the wind turbine. Hence, further research on the impact of aerodynamic elasticity on the wind turbine's response is warranted.

When there are changes in the aerodynamic load on the blades, it is transmitted to the platform through the tower, thereby impacting the entire floating wind turbine system. Following a mooring failure, the sudden alterations in platform motion also affect the aerodynamic load, leading to a complex transient coupling process. Ren et al. [26] conducted simulations using NREL FAST and WAMIT numerical tools to analyze the dynamic response of a 5MW TLP FOWT with mooring failure. The research findings indicate that, under the accidental limit state (ALS), the response of the FOWT is significant, with an average safety factor for mooring of 2.04, satisfying the recommended value in design standards. Yang et al. [27] investigated the nonlinear dynamic characteristics of mooring failure under normal operation and emergency shutdown conditions, employing FAST and AQWA. The study revealed a 156% increase in maximum tension in the remaining mooring lines and a 162% expansion in the range of platform pitch variations. Bae et al. [28] analyzed time-domain variations of mooring through coupled nonlinear dynamic analysis, examining the response of a semi-submersible wind turbine after a single mooring line failure. The results demonstrated that the response of the semi-submersible wind turbine varied based on the mooring pattern, position of the failed mooring line, and direction of environmental loads. Yang et al. [29] developed a fully nonlinear model to calculate the dynamic response of a semi-submersible wind turbine, finding that the third stage after mooring failure typically exhibited the largest pitch. Subbulakshmi et al.[30] explores the application of a tuned mass damper (TMD) for reducing the transient response of FOWT during the mooring line failure. Tang et al. [31] experimented by mounting a 1/64 scale model of the FOWT during a mooring line failure. The results showed that the potential flow-based numerical model overestimated the dynamic response. Neisi et al. [32] investigated the impact of multi-segment mooring system failure on the dynamic motions of the floating platform. They discovered the effectiveness of the buoy multi-clump weight (BMW) as a novel concept to reduce platform hydrodynamic response. It is important to note that the aforementioned studies focused on overall performance after the failure of a single mooring line. However, with long-term operation of floating wind turbines, the mooring system undergoes fatigue and wear, resulting in reserve tension values significantly lower than the design requirements. In extreme ocean loading conditions, mooring failure may trigger a rapid increase in tension in adjacent mooring lines, thereby inducing a cascading failure of multiple mooring lines.

Extensive research on multiple mooring line failures in offshore oil and gas platforms has been conducted, providing valuable insights for studying similar scenarios in FOWTs. Mansour et al. [33] simulated the dynamic response of a TLP platform, specifically examining the transition from intact mooring to complete failure, and validated their results using experimental data. Their study addressed uncertainties in TLP design under harsh environmental conditions. Ahmed et al. [34] discovered that when two mooring lines fail, the drift distance of a Spar platform increases threefold, highlighting the substantial impact of mooring failure on platform motion. Yu et al. [35] analyzed the process of simultaneous and sequential failures of TLP mooring systems under extreme ocean

conditions. It was observed that when mooring failure occurs in the direction of incident waves, subsequent failures of the remaining mooring lines can be triggered, potentially leading to platform overturning. Additionally, the study indicated that the response of the TLP is greater when the failed mooring lines are concentrated in specific locations. These findings hold significant importance in understanding and studying multiple mooring line failures in FOWTs.

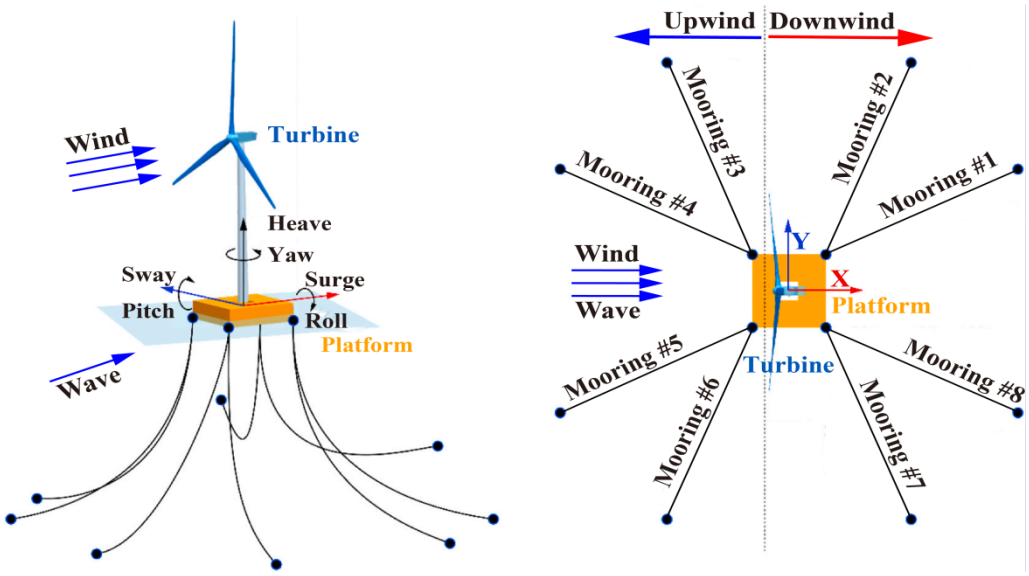
It is important to highlight that existing research on multiple mooring line failures has primarily focused on TLP. The Barge-type platform, thanks to its buoyancy-based stabilization, presents significant advantages compared to other FOWT platforms: lower weight, cost, and construction complexity [36]. Its structural simplicity, ease of modeling, and commercial viability make the Barge-type platform a popular choice in various FOWT design studies [37]. Zhang et al [38]. examined the dynamic reactions and mooring line failure analysis of a floating wind turbine during a typhoon. They discovered that even if the same sort of mooring fails repeatedly on the same side, the entire structure stays stable and does not overturn. Chuang et al. [39] conducted both experiments and numerical analyses on Barge platform wind turbines to investigate their dynamic response characteristics. Notably, Barge platforms have demonstrated the ability to achieve higher wind energy capture efficiency within wind fields [40][41]. However, given their higher overall center of gravity and larger exposed area to incoming waves, Barge platforms must withstand significant wave loads [42].

Hence, this study introduces a novel coupling method utilizing the FAST and AQWA tools (F2A) to investigate the issue of dual mooring line failures specifically in Barge platforms.Considering the diverse locations of mooring line failures and the impact of environmental conditions, this study comprehensively simulated the entire time-domain response process in both rated and extreme sea conditions. The central objective was to thoroughly examine and juxtapose the dynamic responses of wind turbine platforms when encountering dual mooring line failures either on the same side or in the same corner. A comprehensive time-domain response analysis is conducted for both rated sea conditions and extreme sea conditions. Moreover, the timing of the second mooring line failure is carefully adjusted to assess the impact of different time intervals on the platform's motion response and the corresponding changes in mooring line tension. Section 2 introduces the coupling analysis method, followed by Section 3 which thoroughly examines and compares the dynamic response of the platform along with the remaining mooring line tensions under both rated sea conditions and extreme sea conditions. Lastly, the main conclusions derived from this study are presented in Section 4.

2 Fully Coupled Modeling

2.1 Model description and Load cases

The ITI Energy barge is a floating platform that was designed by the Department of Naval Architecture, Ocean & Marine Engineering at the Universities of Glasgow, Strathclyde and Scotland, UK. This Barge is part of a project conducted in collaboration with ITI Energy [16]. The distinguishing feature of the ITI barge platform is its square-type floater. It incorporates a sophisticated mooring system consisting of eight mooring lines, with two lines situated at each corner of the platform's base, ensuring precise positioning and orientation. For ease of description, the mooring lines are numbered as 1 to 8. As shown in Fig. 2, mooring lines 1 and 2 are located in the first quadrant, while the remaining mooring lines are arranged sequentially. Both the wind and wave loads propagate in the positive direction along the X-axis. Table 1 provides an overview of the characteristics of the Barge platform and its mooring system [43].



（a）Isometric view　　（b）Top view

Fig. 2 The NREL 5 MW wind turbine supported by the barge platform

Table 1

Barge platform parameters

Property	Value	Unit
Diameter or width × length	40 × 40	(m)
Draft	4	(m)
Water displacement	6,000	(m^3)
Mass, including ballast	5,452,000	(k·g)
CM location of the platform below SWL	0.2818	(m)
Roll inertia about CM	726,900,000	($kg·m^2$)
Pitch inertia about CM	726,900,000	($kg·m^2$)
Yaw inertia about CM	1,454,000,000	($kg·m^2$)
Number of mooring lines	8	(-)
Depth to fairleads, anchors	4, 150	(m)
Radius to fairleads, anchors	28.28, 423.4	(m)
Unstretched line length	473.3	(m)
Line diameter	0.0809	(m)
Line mass density	130.4	($kg·m^{-1}$)
Breaking load	72,000,000	(*N*)

To investigate the performance of the wind turbine under different scenarios, two specific sets of wind-wave coupling conditions were selected for simulation. These conditions include the rated condition for the NREL 5 MW wind turbine and an extreme marine environment representing a 50-year return period in the South China Sea. In our study, we chose the well-documented NREL 5MW wind turbine model, which epitomizes a typical three-bladed, upwind design[44]. This model is widely recognized in wind energy research and provides a standard benchmark, making it ideal for assessing the ITI Energy barge under various wind and wave conditions.

To examine the impact of mooring line failures on the wind turbine's performance, simulations were conducted with different scenarios. Specifically, the failure of mooring lines #4 and #5 on the

upwind side, as well as the failure of mooring lines #5 and #6 in the same corner, were investigated. The failure intervals were set to three different values: 0s, 60s, and 1500s. A failure interval of 0s represents the simultaneous failure of two mooring lines. Based on the simulation results, it was observed that after the failure of one mooring line, the platform reached its peak surge motion after approximately 60s. Since surge motion has the most significant impact on the platform, the second mooring line was set to fail after a 60-second interval to test the platform's stability under the most severe conditions. After the failure of one mooring line for a duration of 1500s, the wind turbine reached an equilibrium state. The simulation results were used to compare the dynamic response between the failure of one mooring line and the failure of two mooring lines. The total simulation time was set to 4000s and divided into three stages. The first stage ranged from 0s to 1500s, representing the intact mooring phase. At 1500s, the first mooring line failed, marking the beginning of the second stage. The second stage continued until the failure of the second mooring line. The third stage commenced after the failure of both mooring lines. By analyzing the wind turbine's performance under these different mooring failure scenarios and intervals, valuable insights into the system's behavior and stability can be gained.

To investigate the performance of the NREL 5 MW wind turbine in different environmental conditions, two wind and wave coupling scenarios were selected: the rated sea condition and an extreme ocean environment with a 50-year return period in the South China Sea [45]. Irregular waves were simulated based on the P-M wave spectrum [46], characterized by significant wave height H_S and spectral peak period T_z. The wind field was generated using the IEC Kaimal wind spectrum [47]and TurbSim [48].

The P-M spectrum, derived from long-term data measured in the North Atlantic and analyzed statistically, is widely used to analyze ocean platforms in fully developed, infinite wind regions. This makes it particularly suitable for analyzing floating wind turbines in deep-sea environments. The spectral expression is given by:

$$S(\omega) = 4\pi^3 \frac{H_S^2}{T_Z^4} \frac{1}{\omega^5} \exp\left(-\frac{16\pi^3}{T_z^4} \frac{1}{\omega^4}\right) \quad (1)$$

where H_s represents significant wave height m; T_z is the mean zero-crossing period s; ω denotes the phase deg.

Due to the strong randomness of turbulent wind spectra, especially in the power spectral density function of turbulent wind from different directions, these are often used to characterize its statistical properties. In this study, the Kaimal spectrum, suitable for a neutral atmospheric environment, is selected and can be expressed as:

$$s_k(f) = \frac{4\sigma_k^2 L_k / u_{hub}}{(1 + 6fL_k / u_{hub})^{1.67}} \quad (2)$$

where S_k represents the one-sided spectrum of the velocity component m/s; f represents frequency in Hz; k denotes the index of the three velocity components (1-longitudinal u, 2-lateral v, 3-vertical w); σ_k denotes the standard deviation of the velocity component m/s; L_k signifies the turbulence integral scale parameter of the velocity component m/s; U_{hub} refers to the wind speed at the hub of the wind turbine m/s.

Different combinations of wind and wave conditions were considered in this study, leading to the definition of 14 distinct sets of Load Cases (LCs). Specifically, LC 1 to LC 6 represented the rated conditions, while LC 7 to Load LC 12 represented extreme conditions. Notably, LC 10 and

LC 11 were characterized by the complete failure of all mooring lines, resulting in platform overturning under those specific circumstances. To further explore the intricate dynamics of mooring line failure during emergency shutdown scenarios, LC 13 and LC 14 were devised. In these load cases, the wind turbine was deliberately set to a shutdown state while maintaining the other conditions unchanged. For a more comprehensive understanding of the specific wind speeds, wave characteristics, mooring line failures, and corresponding wind turbine behavior in each load case, please consult Table 2.

Table 2

Definitions and parameters of selected environmental conditions.

Load cases	V_{Hub} /m·s^{-1}	H_S /m	T_p /s	Time intervals /s	Failed moorings	Description	Turbine status
LC1	11.4	3	10	0	4,5	Rated condition	Operating
LC2	11.4	3	10	60	4,5	Rated condition	Operating
LC3	11.4	3	10	1500	4,5	Rated condition	Operating
LC4	11.4	3	10	0	5,6	Rated condition	Operating
LC5	11.4	3	10	60	5,6	Rated condition	Operating
LC6	11.4	3	10	1500	5,6	Rated condition	Operating
LC7	40	14.1	15	0	4,5	50-year extreme condition	Operating
LC8	40	14.1	15	60	4,5	50-year extreme condition	Operating
LC9	40	14.1	15	1500	4,5	50-year extreme condition	Operating
LC10	40	14.1	15	0	5,6	50-year extreme condition	Operating
LC11	40	14.1	15	60	5,6	50-year extreme condition	Operating
LC12	40	14.1	15	1500	5,6	50-year extreme condition	Operating
LC13	40	14.1	15	0	5,6	50-year extreme condition	Parked
LC14	40	14.1	15	60	5,6	50-year extreme condition	Parked

2.2 Dynamic Modeling of Mooring System

During the analysis of mooring systems, it is of utmost importance to take into account factors such as corrosion margin and redundancy. These considerations significantly contribute to the reliability and safety of the system [49]. The safety factor of mooring tensions relies on the design conditions and the specific mooring analysis method employed [50]. When a mooring system experiences failure, two conditions must be satisfied: firstly, after the mooring line failure, the FOWT must oscillate around a new equilibrium position to ensure the stability of the system; secondly, prior to reaching the new equilibrium position, the FOWT must undergo transient motion to adapt to the changes within the system. In accordance with the requirements outlined in Table 3, the safety factor F of mooring tensions should exceed a predefined threshold [51][52]. The formula for calculating the tension safety factor F is as follows:

$$F = P_B / T_{\max} \tag{3}$$

where P_B represents the minimum rated breaking load of the mooring, kN; T_{max} represents the maximum tension in the mooring, kN。

Table 3

Safety factors for mooring systems

Classification society	Materials of mooring lines	Whether consider transient response	Safety factor	Design sea state
	Steel	No	1.05	50-year

ABS	Synthetic fiber	Yes	1.05	sea state
ClassNK	Steel	No	1.25	At least 1-year sea state
	Synthetic fiber	Yes	1.05	
	Steel	No	1.88	
	Synthetic fiber	Yes	1.58	

In Aqwa [12], a dynamic analysis method is utilized to model the mooring system. This approach involves discretizing each mooring line into multiple finite element units, with the mass of each unit concentrated at a specific node. The analysis takes into account various factors, including mooring mass, resistance, elastic forces, and moments. Given the nonlinear nature of the mooring system's dynamic response, tension values vary over time. An interaction between the mooring and the platform occurs, with the mooring tension restricting the platform's motion, and the platform's motion, in turn, influencing the mooring tension. Moreover, nonlinear springs and dampers are incorporated to simulate the seabed's effect. Through time integration, the tension in the mooring can be computed.

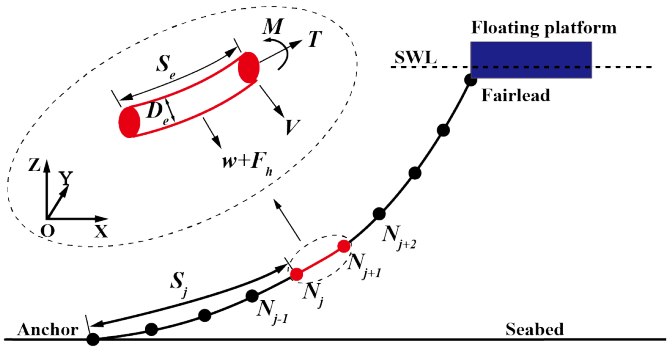


Fig. 3 Schematic diagram of the dynamic model of a mooring line

In Fig. 3 S_j represents the unstretched length between the anchor point and the *j*th-node, and *De* represents the diameter of the local segment of the mooring line. $\boldsymbol{w}$ symbolizes the gravitational force per unit length of the element. Each catenary segment is considered uniform. The segment characteristics are described in a mooring local axis system, where the local x-axis is a projection onto the seafloor of the vector connecting the two attachment points, and the local z-axis points vertically upwards. At the origin, the catenary line profile maintains zero slope, i.e., dY/dX=0[53].

The equation of motion for a specific element of the mooring line, modeled as a Morrison-type element subject to external forces[12], can be expressed as follows:

$$\frac{\partial \boldsymbol{T}}{\partial S_e}+\frac{\partial \boldsymbol{V}}{\partial S_e}+\boldsymbol{w}+\boldsymbol{F_h}=m_e\frac{\partial^2 \boldsymbol{R}}{\partial t^2} \tag{4}$$

$$\frac{\partial \boldsymbol{M}}{\partial S_e}+\frac{\partial \boldsymbol{R}}{\partial S_e}+\boldsymbol{V}=\mathbf{-q} \tag{5}$$

where $\boldsymbol{T}$ is the tension force vector at the first node of the element kN, S_e represents an arbitrary element of the mooring line, $\boldsymbol{V}$ is the shear force vector at the first node of the element kN-m, $\boldsymbol{w}$ is the gravity vector per unit length of the element kN, $\boldsymbol{F_h}$ is the external hydrodynamic load applied to per unit length of the element kN, m_e is the mass of per unit length kg, $\boldsymbol{R}$ is the position vector of the first node m, $\boldsymbol{M}$ is the bending moment vector at the first node of the element kN·m, $\boldsymbol{q}$ is the distributed moment load per unit length of the element kN·m.

The tension $\boldsymbol{T}$ and bending moment $\boldsymbol{M}$ experienced by each segment can be respectively expressed as:

$$\boldsymbol{T}=EA\cdot\varepsilon \tag{6}$$

$$\boldsymbol{M} = EI \cdot \frac{\partial R}{\partial S_e} \times \frac{\partial^2 R}{\partial S_e^{\,2}} \tag{7}$$

where *EI* and *EA* are the bending stiffness and axial stiffness of the mooring line N/m, and $\varepsilon$is the axial strain of the mooring line.

2.3 The coupling model

The FOWT operates within the complex marine environment, when subjected to the force of wave loads, the floating platform undergoes intricate oscillations, thereby inducing a rhythmic swaying motion in the wind turbine rotor. This dynamic interaction gives rise to fluctuations in the inflow of wind, subsequently eliciting alterations in the aerodynamic loads experienced by the system.These load variations are transmitted through the tower structure to the floating platform, impacting the entire system of the floating wind turbine. To address this issue, the combined capabilities of the FAST [54] software in aerodynamic-servo-structural analysis and the AQWA software in hydrodynamic analysis are synergistically utilized. By modifying the user_force.dll and FAST subroutine source code, the AQWA software is enhanced to invoke the relevant simulation functionalities of FAST through DLL calls. This enables the computation of the coupled relationship between the dynamic response of the upper structure of the floating wind turbine and the lower platform. The coupled framework has undergone thorough validation and has been successfully employed in the coupled dynamic analysis of offshore wind turbines [55][56]. Fig. 4 presents the flowchart of the coupled model.The simulation is examined through the following steps:

(1) Initialize the platform responses in the AQWA program.

(2) Calculate aerodynamic loads on the blades in Fast.

(3) Invoke the DLL to update the kinematics of the tower, nacelle, and blades.

(4) Transfer the tower-base loads obtained in the user-force.dll into the AQWA program.

(5) Compute the platform's dynamic response based on the tower-base loads from the DLL, hydrodynamic loads, and mooring restoring forces on the platform.

(6) Repeat steps (2) – (5) until the termination of the simulation.

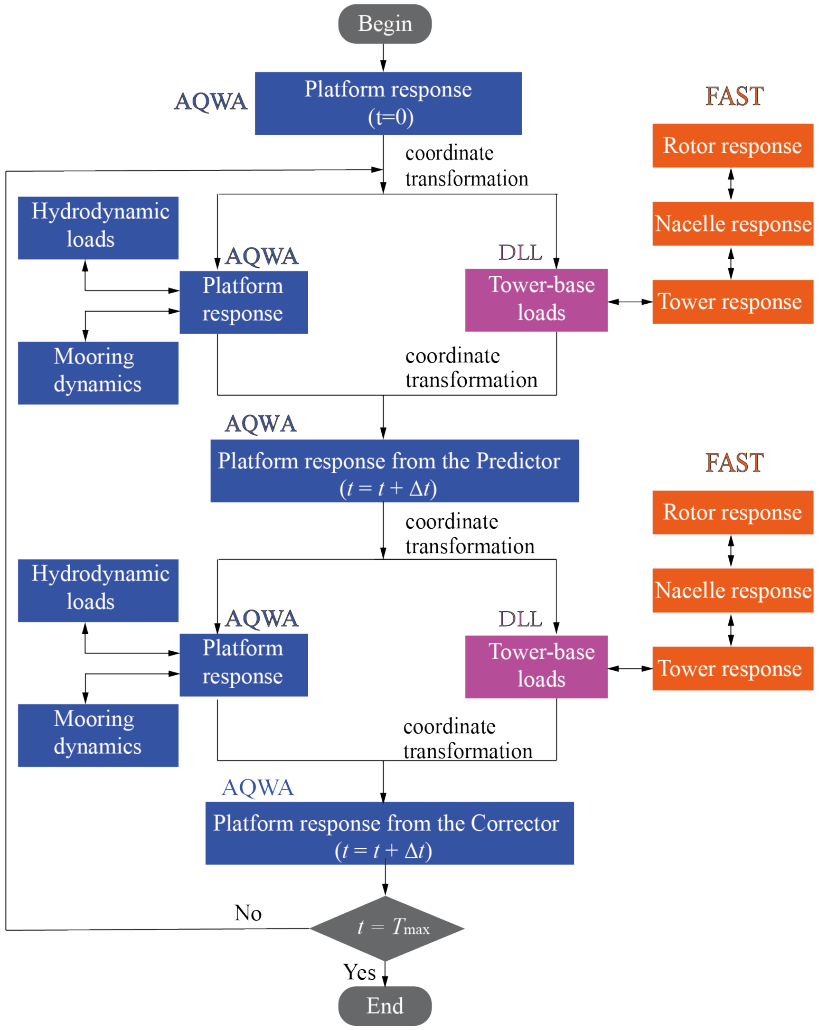


Fig.4 Calculation flowchart of the numerical simulation.

The combined utilization of these software tools enables a time-domain analysis of the system. AQWA, employing a predictor-corrector algorithm, adeptly determines the position, velocity, and acceleration of the platform. These computed parameters are subsequently communicated to the FAST module, facilitating the simulation of the dynamic response of the upper structure, encompassing the blades and tower. Furthermore, the resultant loads at the tower base are imported into AQWA as external forces. The DLL is invoked twice at each time step to effectively achieve the coupling calculation between the platform's response and the aerodynamic loads acting upon the upper structure. The motion equation governing the floating platform can be expressed as follows[21]:

$$\mathbf{M}\ddot{\mathbf{X}}(t) + \mathbf{C}\dot{\mathbf{X}}(t) + \mathbf{K}\mathbf{X}(t) + \int_0^t \mathbf{h}(t-\tau)\ddot{\mathbf{X}}(\tau)\mathrm{d}\tau = \mathbf{F}(t) \tag{8}$$

Where **M** is the mass matrix of the platform composed of the inertia mass and added mass kg. $\mathbf{X}(t)$, $\dot{\mathbf{X}}(t)$, and $\ddot{\mathbf{X}}(t)$ are the displacement, velocity, and acceleration vectors of the platform at time t, respectively m, m/s, m/s^2 . **F(*t*)** is the total external force vector including the total hydrodynamic and mooring load vectors kN. ***C*** and ***K*** are the total damping and stiffness matrices N/m, respectively. ***h(t)*** is the acceleration impulse response matrix, which is used to examine the radiation memory effects and defined as follows:

$$\mathbf{h}(t) = \frac{2}{\pi}\int_0^{\infty} \mathbf{B}(\omega)\frac{\sin(\omega t)}{\omega}\mathrm{d}\omega \tag{9}$$

Where $\mathbf{B}(\omega)$ represents the radiation attenuation at a wave frequency of ω Hz.

To ensure precise coupling of the dynamic responses between the platform and the upper structure, a coordinate transformation becomes essential, given that these two components employ different coordinate systems. In AQWA, the position, velocity, and acceleration of the platform's center of gravity are computed in the inertial coordinate system. Conversely, FAST simulates the dynamic response of the upper structure using a local coordinate system anchored at the tower base Fig. 5 illustrates the schematic diagram of the coordinate transformation.

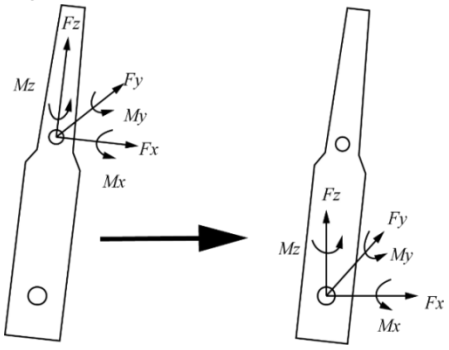


Fig. 5 Coordinate transformation

The transformation of the platform position and velocity vectors from the inertial coordinate system to the local coordinate system utilized in the FAST module requires the use of a transformation matrix. This matrix can be expressed as follows:

$$\boldsymbol{T}_{mat}=\begin{bmatrix} \dfrac{\theta_1^2\sqrt{1+s}+\theta_2^2+\theta_3^2}{s\sqrt{1+s}} & \dfrac{\theta_3 s+\theta_1\theta_2(\sqrt{1+s}-1)}{s\sqrt{1+s}} & \dfrac{-\theta_2 s+\theta_1\theta_3(\sqrt{1+s}-1)}{s\sqrt{1+s}} \\ \dfrac{-\theta_3 s+\theta_1\theta_2(\sqrt{1+s}-1)}{s\sqrt{1+s}} & \dfrac{\theta_2^2\sqrt{1+s}+\theta_1^2+\theta_3^2}{s\sqrt{1+s}} & \dfrac{\theta_1 s+\theta_2\theta_3(\sqrt{1+s}-1)}{s\sqrt{1+s}} \\ \dfrac{\theta_2 s+\theta_1\theta_3(\sqrt{1+s}-1)}{s\sqrt{1+s}} & \dfrac{-\theta_1 s+\theta_2\theta_3(\sqrt{1+s}-1)}{s\sqrt{1+s}} & \dfrac{\theta_3^2\sqrt{1+s}+\theta_1^2+\theta_2^2}{s\sqrt{1+s}} \end{bmatrix} \tag{10}$$

where: θ_1, θ_2 and θ_3 are the roll, pitch and yaw angles of the platform deg, respectively. s is equal to $\theta_1{}^2+\theta_2{}^2+\theta_3{}^2$ 。

For an accurate simulation of the dynamic response in the multi-physics analysis of FOWTs, it is crucial to correct the translation velocity of the platform before passing it to the FAST module. This correction becomes necessary when the reference point of the platform, defined as the origin of the inertial coordinate system (0, 0, 0), is used in FAST. The corrected translation velocity of the platform can be determined using the following equation:

$$\begin{bmatrix} V_x \\ V_y \\ V_z \end{bmatrix}=\begin{bmatrix} U_x \\ U_y \\ U_z \end{bmatrix}-\mathbf{T}_{\text{mat}}\cdot\begin{bmatrix} \text{CoG}_x \\ \text{CoG}_y \\ \text{CoG}_z \end{bmatrix}\times\begin{bmatrix} \omega_x \\ \omega_y \\ \omega_z \end{bmatrix} \tag{11}$$

Where $[V_x, V_y, V_z]^{\mathrm{T}}$ is the platform velocity vectors obtained in the DLL; $[U_x, U_y, U_z]^{\mathrm{T}}$ is the platform velocity vectors obtained in AQWA; $[\omega_x, \omega_y, \omega_z]^{\mathrm{T}}$ is the rotational velocity vector of the platform obtained in AQWA; $[\mathrm{CoG}_x, \mathrm{CoG}_y, \mathrm{CoG}_z]^{\mathrm{T}}$ is the position vector from the reference point to the mass center of the platform.

To ensure accurate load transfer from FAST to AQWA, it is necessary to correct the loads obtained from FAST. This correction involves converting the translational and rotational loads at the tower base from the local coordinate system used in FAST to the inertial coordinate system used in AQWA. The conversion process can be expressed mathematically as follows:

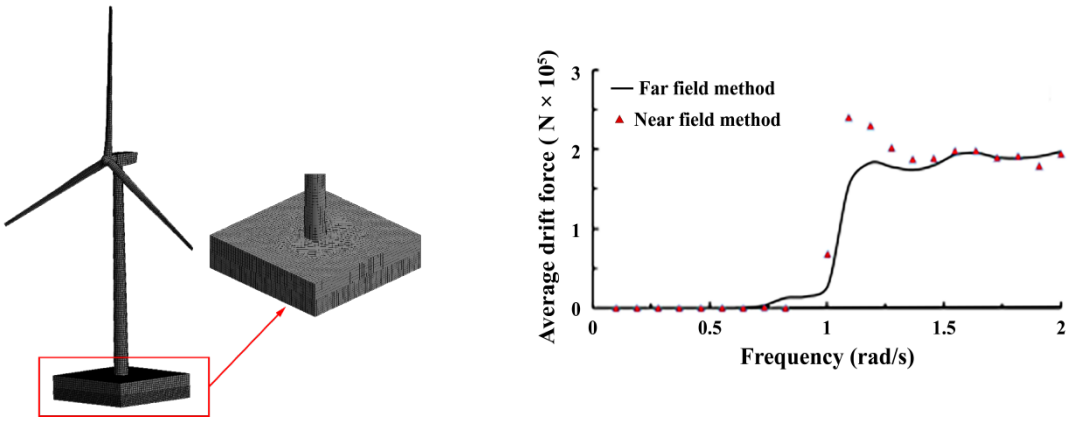
$$\boldsymbol{F}_{AQWA} = \boldsymbol{T}_{mat}^{-1} \cdot \boldsymbol{F}_{FAST} \tag{12}$$

$$\boldsymbol{M}_{AQWA} = \boldsymbol{T}_{mat}^{-1} \cdot (\boldsymbol{M}_{FAST} - \boldsymbol{CoG} \times \boldsymbol{F}_{FAST}) \tag{13}$$

where: $\boldsymbol{F}_{AQWA}$ and $\boldsymbol{F}_{FAST}$ are the translational force vectors in AQWA and FAST, respectively; $\boldsymbol{M}_{AQWA}$ is the moment vector acting at the platform's mass center with respect to the inertial coordinate system. $\boldsymbol{M}_{FAST}$ is the moment vector acting at the tower-base with respect to the platform's local coordinate system obtained in the FAST.

The Barge platform was divided into a mesh, and the diffraction elements on the wet surface were refined. The maximum grid size above the waterline was set to 1 m, and below the waterline, it was set to 0.5 m. Approximately 8000 grids were generated, including around 5000 diffraction grids, as illustrated in Fig. 6(a). The computation time was set to 4000s, with a time step of 0.1s, totaling 40000 steps.

The second-order wave loads on the platform obtained through near-field and far-field methods are shown in Fig. 6(b) [57]. The loads acting on the barge platform peak around the wave frequency of 1.2 rad/s and stabilize after reaching the peak. Additionally, the results obtained by the far-field and near-field methods are consistent, indicating that the mesh division meets the accuracy requirements [58].



(a) (b)

Fig. 6 Mooring tensions under three LCS.

The turbulent wind field is generated by TurbSim. To ensure the upper wind turbine rotor consistently remains within this turbulent wind field during operation, it is necessary to ensure that the size of the turbulent wind field is designed to be at least 10% larger than the rotor diameter. Considering the potential for larger displacements in floating wind turbines, the turbulent wind field is set with a horizontal width and vertical height of 150m, centered on the hub of wind turbine rotor. This design maintains the rotor within the wind field. For a balance between computational efficiency and accurate turbulence representation, the wind field is divided into a 31×31 grid area.

The computational work for this study was conducted on the high-performance computing cluster at Shanghai University of Science and Technology, featuring a peak CPU performance of 260.915 Tflops, 110 nodes, 3136 cores, GPU capabilities of 112 Tflops, and 924 TB storage. The AQWA analysis, part of ANSYS 2020 suite, took 77 minutes, while the OpenFAST 3.5.0 simulations for wind turbine analysis required 147 minutes, totaling 224 minutes of runtime.

3 Calculation Results

3.1. Validation of F2A

The novel coupling methodology of F2A underwent validation using OpenFAST 3.5.0,. To optimize the comparison, we focused on the platform's surge, sway, and the upwind mooring lines #4 and #5, as these parameters display the most substantial variations during the simulation.

In Fig. 7, the coupled response of the FOWT, as predicted by F2A and OpenFAST, is presented. It is evident that the surge and sway calculated by F2A closely mirror the changing trends observed in OpenFAST throughout the entire simulation process, exhibiting nearly identical statistical characteristics. These comparisons suggest that the disparities between the results obtained from these tools can be considered negligible.

The tension in mooring lines #4 and #5, as predicted by F2A, aligns considerably well with the results from OpenFAST, albeit with slight variations in magnitude. The extreme values predicted by F2A are marginally smaller, primarily attributed to inherent disparities in the mooring system modeling. Following a meticulous comparison, the results derived from F2A are deemed acceptable.

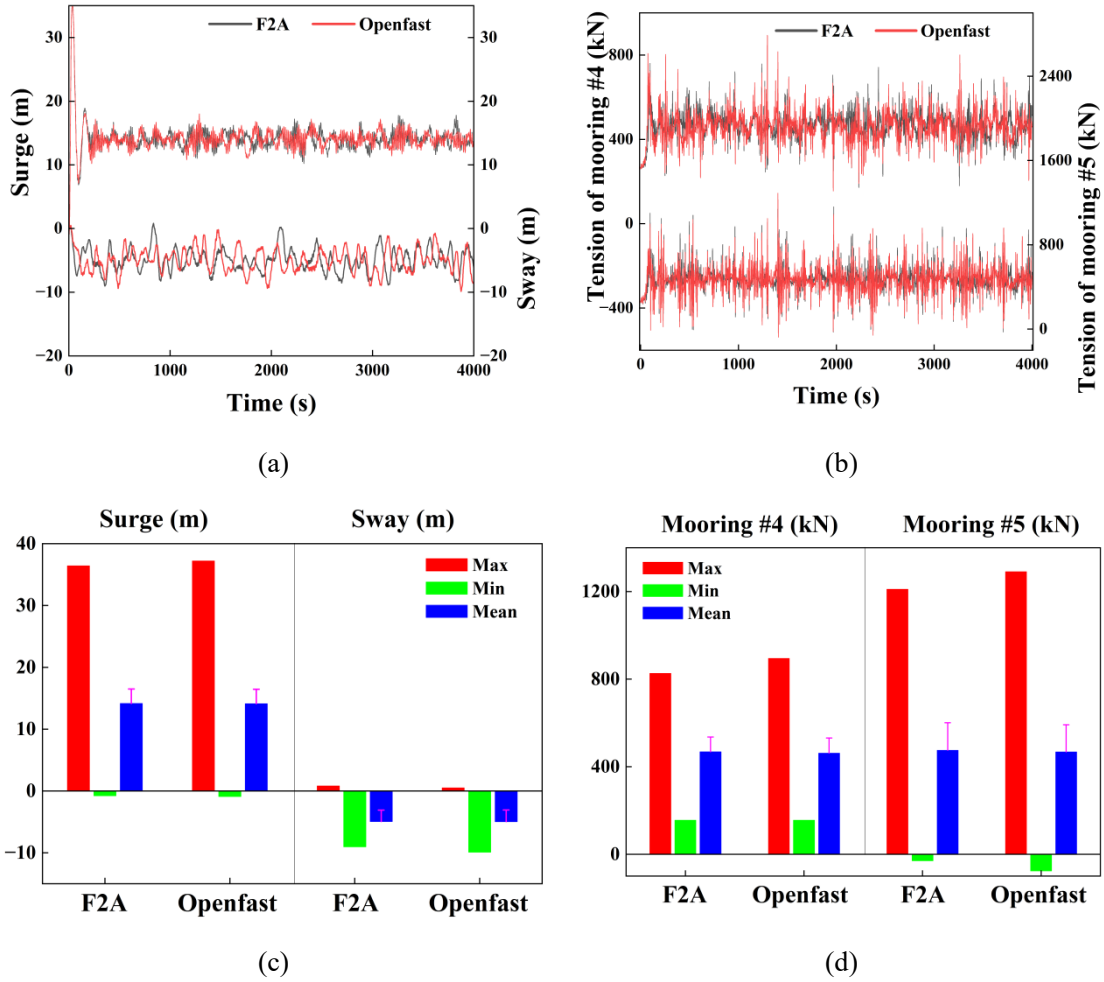


Fig. 7 Comparison between coupled responses of F2A and OpenFAST.

3.2 Rated sea conditions

In this section, an analysis is conducted on the dynamic response of the platform and the variations in tension in adjacent mooring lines after the failures of mooring lines under rated sea conditions. The study also explores the patterns of characteristic values at each stage.

3.2.1 The dynamic response of the platform

The motion of the platform encompasses translational movements such as surge, sway, and heave, as well as rotational motions including roll, pitch, and yaw. By evaluating the eigenvalues at each stage, it becomes possible to delve deeper into the platform's motion characteristics. To explore the transient effects of the wind turbine, we examined the trajectory of its center of gravity and analyzed local time-domain plots.

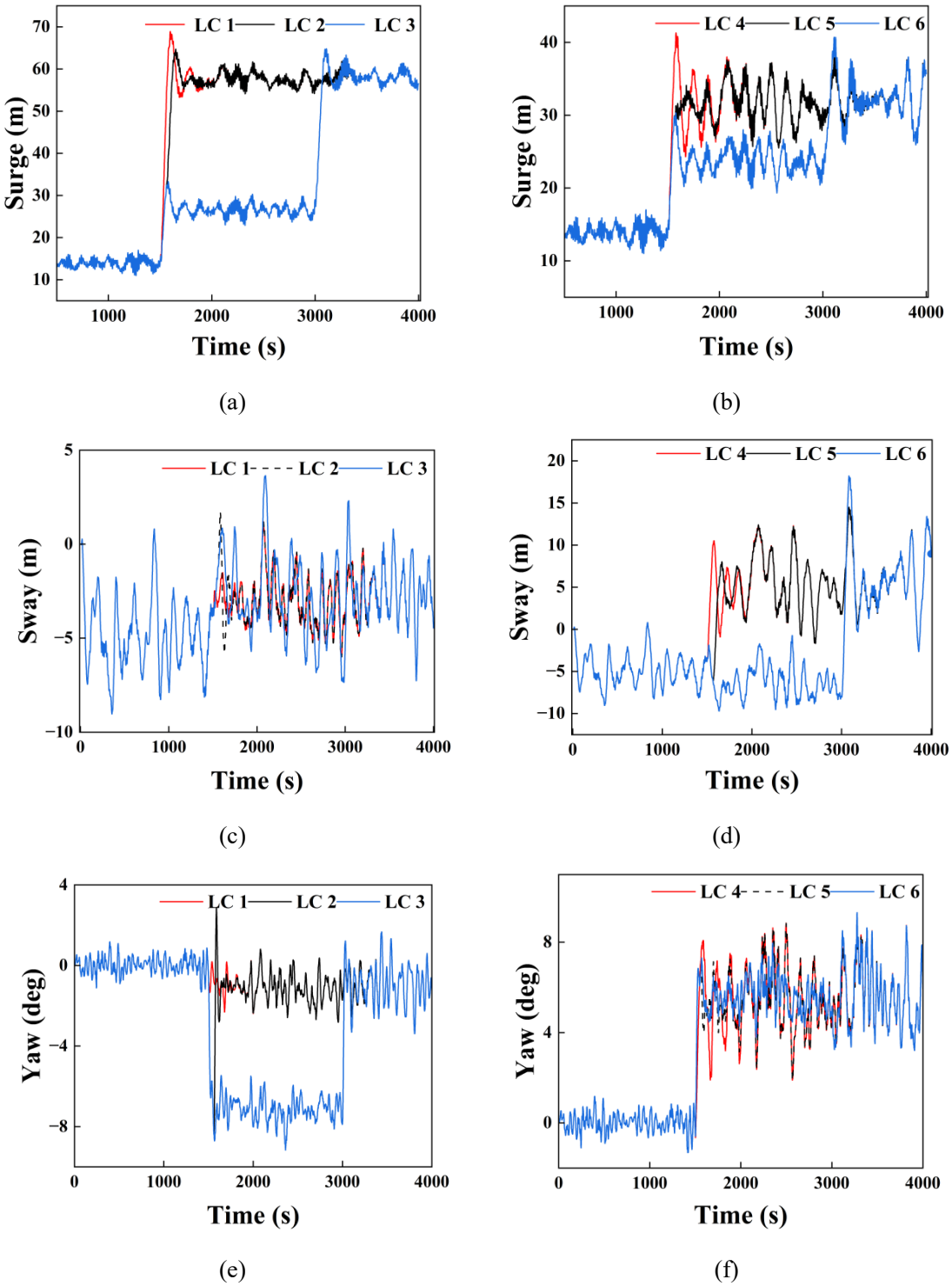


Fig. 8 Platform motions in rated sea conditions

In the event of mooring system failure, the dynamic response of the platform undergoes

significant changes. Before the failure, the loads exerted by both the mooring system and environmental forces reach a state of dynamic equilibrium. However, when a mooring failure transpires, the tension experienced by the platform diminishes while the environmental forces continue to exert their influence relatively unchanged, at least in the short term. This imbalance disrupts the stability of the platform, leading to the onset of drift and rotation.

In the scenario where two mooring failures occur, the platform's heave, roll, and pitch exhibit minimal changes across the three stages. However, substantial variations are observed in the platform's surge, sway, and yaw. To facilitate a comprehensive comparison, Fig. 8(a), (c), and (e) showcase the platform's surge, sway, and yaw following the failure of mooring lines #4 and #5, respectively. Likewise, Fig. 8(b), (d), and (f) present the platform's surge, sway, and yaw after the failure of mooring lines #5 and #6, respectively. A noteworthy trend is the notable increase in the amplitude of the response curves subsequent to the failures. This increase signifies a significant reduction in the overall stability of the wind turbine system.

Based on the observations from Fig. 8(a) and (b), we can draw the following conclusions: In the event of mooring lines #4 and #5 failure, the platform experiences a significant surge motion. This is primarily due to the acute angles formed by mooring lines #4 and #5 with the wind and wave loads. These acute angles restrict the platform's motion along the positive X-axis, leading to an increased surge motion. Conversely, mooring line #6 forms an acute angle with the Y-axis, resulting in a larger component of tension in the sway direction. Therefore, when mooring lines #5 and #6 fail, the platform exhibits a more pronounced sway motion, as observed in Fig. 8(c) and (d).

A distinct difference in response trends is observed when the interval between the two mooring failures is 1500s (LC 3 and LC 6). In the surge direction, the response curve exhibits a stepped increase. In the sway direction, as depicted in Fig. 8(d), the response curve after the failure of mooring line #5 shows no significant changes, whereas after 3000s, the failure of mooring line #6 results in a noticeable increase in sway. This further demonstrates the greater impact of mooring line #6 failure on sway motion.

Comparing the yaw motions of the platform in Fig. 8(e) and (f), the following conclusions can be drawn: When mooring lines #5 and #6 fail, the platform demonstrates a greater rotational angle in yaw motion. This can be attributed to the asymmetric oscillation of the blades caused by turbulent wind conditions. In the scenario where mooring lines #5 and #6 fail while mooring line #4 remains intact, the platform undergoes a counterclockwise rotation due to the combined effect of wind and wave loads, resulting in a substantial yaw motion.

By observing LC 3 and LC 6, we can understand the impact of a single mooring line failure on yaw motion. In LC 3 of Fig. 8(e), the failure of mooring line #4 at 1500s immediately initiates a yaw motion in the negative direction. Subsequently, at 3000s, after the failure of mooring line #5, the remaining mooring lines are symmetrically distributed along the X-axis, leading to a reduction in uneven mooring line tensions. As a result, the platform undergoes a rotation in the opposite direction, resulting in a decrease in the yaw angle. Similarly, in LC 2 of Fig. 8(e) with a failure interval of 60s, the yaw rotation angle initially decreases and then rapidly increases, following a similar trend. In LC 6 of Fig. 8(f), at 1500s, the failure of mooring line #5 induces a yaw motion in the positive direction. Subsequently, at 3000s, after the failure of mooring line #6, the yaw motion continues to increase, but the rate of increase diminishes, indicating that mooring line #5 has a greater impact on the yaw motion.

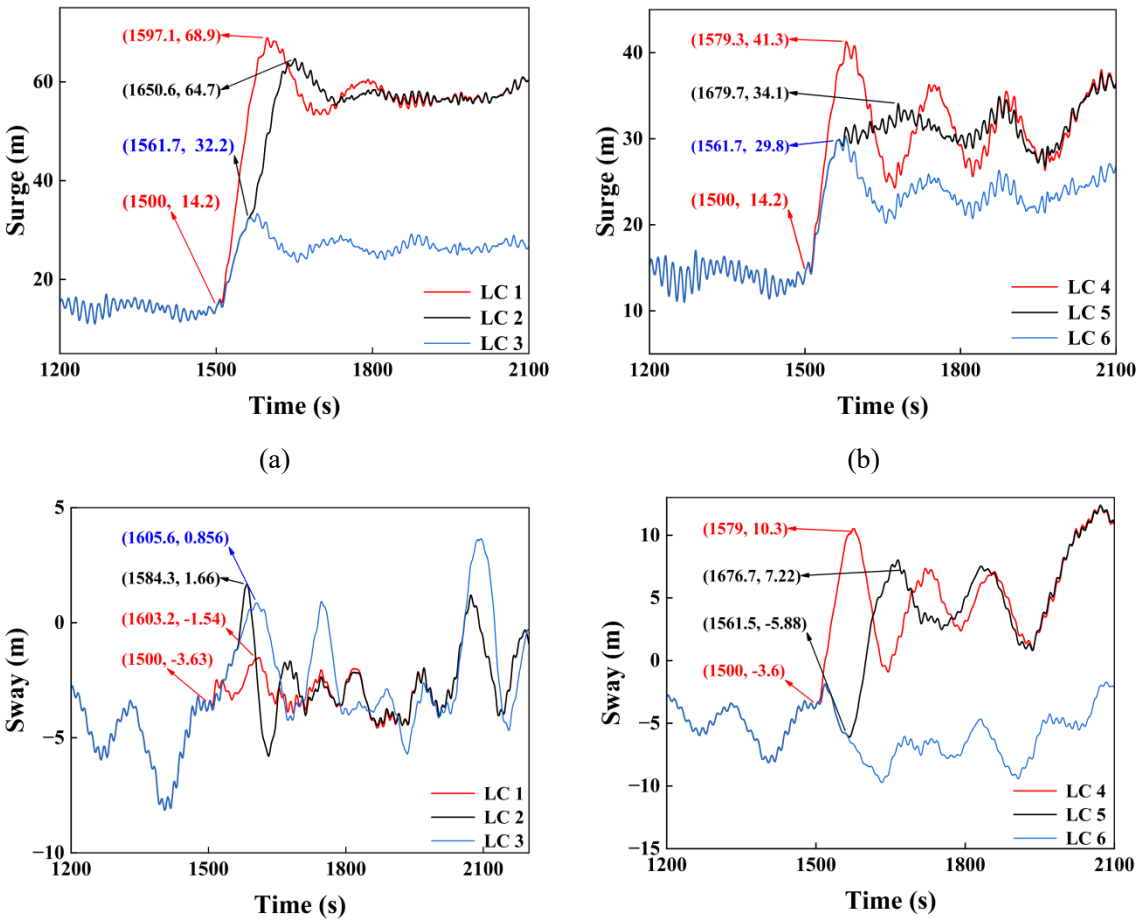


Fig. 9 Local time-domain response in rated sea conditions

To further investigate the transient response of the platform, a localized temporal response graph was depicted in Fig. 9. Specifically, Fig. 9(a) and (c) represent the surge and sway of the platform around 1500s after the failure of mooring line #4 and #5, respectively. Similarly, Fig. 9(b) and (d) illustrate the surge and sway of the platform around 1500s following the failure of mooring line #5 and #6, respectively.

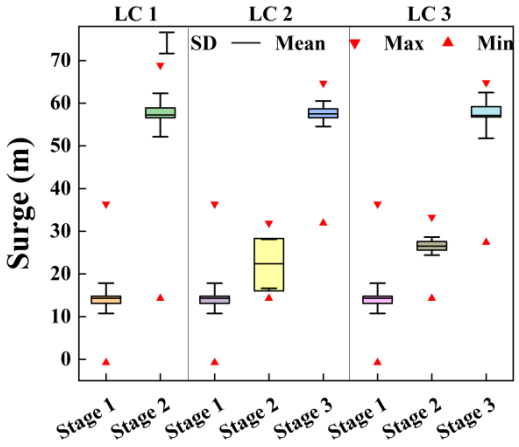
By examining Fig. 9(a) and (b) for LC 3 and LC 6, it can be inferred that after the initial mooring failure at 1500s, the platform reached its first peak of pre-equilibrium at approximately 1561.7s. This indicates that it took approximately 60s for the platform to achieve the maximum surge displacement from its original position following the failure of the initial mooring. Furthermore, the surge motion notably affected the Barge platform. Consequently, in LC 2 and LC 5, the second mooring failure was intentionally scheduled with a 60s interval, allowing for a comprehensive examination of platform stability.

Comparing LC 1, LC 2, and LC 3 in Fig. 9(a), it is observed that in LC 1, where both moorings failed simultaneously at 1500s, the platform reached its first peak at 1597.1s and then entered a stable state. The surge displacement of the platform was 54.7m with a velocity of 0.56m/s. In LC 2, the second mooring failure occurred at 1560s, and the platform reached its first pre-equilibrium peak at 1650.6s, covering a distance of 50.5m with an average velocity of 0.335m/s. In LC 3, the platform moved 18m within 61.7s, with a velocity of 0.292m/s. It can be concluded that when both moorings failed simultaneously, the platform exhibited the fastest drift speed, resulting in high instability of

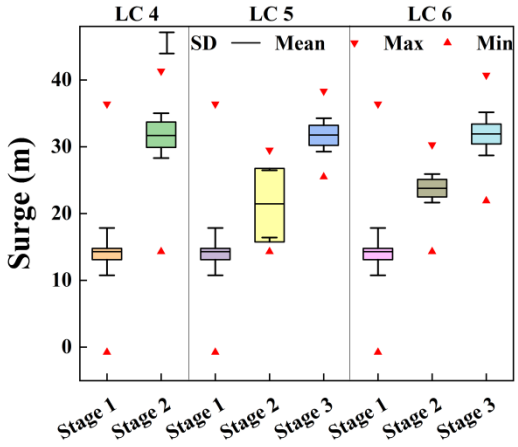
the wind turbine. Conversely, when the two moorings failed with a 60s interval, the disturbances overlapped, leading to a longer time for the wind turbine to reach a new stable state. A similar trend is observed in Fig. 9(b) for LC 4, LC 5, and LC 6. The transient response times for reaching a new equilibrium state were 79.3s, 179.7s, and 61.7s, respectively, with average velocities of 0.342m/s, 0.11m/s, and 0.25m/s, all of which were lower than the previous case. The peak velocity observed in the platform trajectory between 3000 and 4000s can be elucidated as follows: The platform maintains balance through a complex mooring system linked to the seabed. Prior to failure, the system, along with environmental forces, establishes dynamic equilibrium. At 3000s, the failure of two mooring lines reduces the system's restorative force, while wind and wave loads remain constant. Compared to initial stages, external forces on the wind turbine increase significantly, causing more pronounced surge and heave motions. This results in increased velocity in the platform's trajectory during this period.

The trend of sway in Fig. 9(c) differs significantly from the surge observed in Fig. 9(a). In LC 1, where both mooring lines fail simultaneously, the sway exhibits the smallest amplitude and longest duration. In LC 2, as the two mooring lines fail successively, the disturbances accumulate and reach their peak at the fastest rate. Interestingly, in LC 3, the platform's vibration amplitude is actually the largest when only one mooring line fails. This discrepancy can be attributed to the resultant force from the failed mooring lines #4 and #5 being parallel to the direction of the wind and wave loads. When these two mooring lines fail, the platform drifts in the surge direction, causing rapid tension and elongation in the adjacent mooring lines #3 and #6. As a result, the force components in the Y-axis direction increase and oppose each other, thereby limiting the sway motion of the platform. However, when only mooring line #4 fails, the imbalance in forces actually amplifies the sway motion.

On the other hand, the trend of sway in Fig. 9(d) approximately aligns with Fig. 9(b). Prior to the platform reaching a new equilibrium state, corresponding to LC 4, LC 5, and LC 6, the transient response times for sway are 79s, 176.7s, and 61.7s, respectively. This can be attributed to the resultant force from mooring lines #5 and #6 lying along the bisector of the X and Y axes, resulting in the same effect on both surge and sway motions.



(a)



(b)

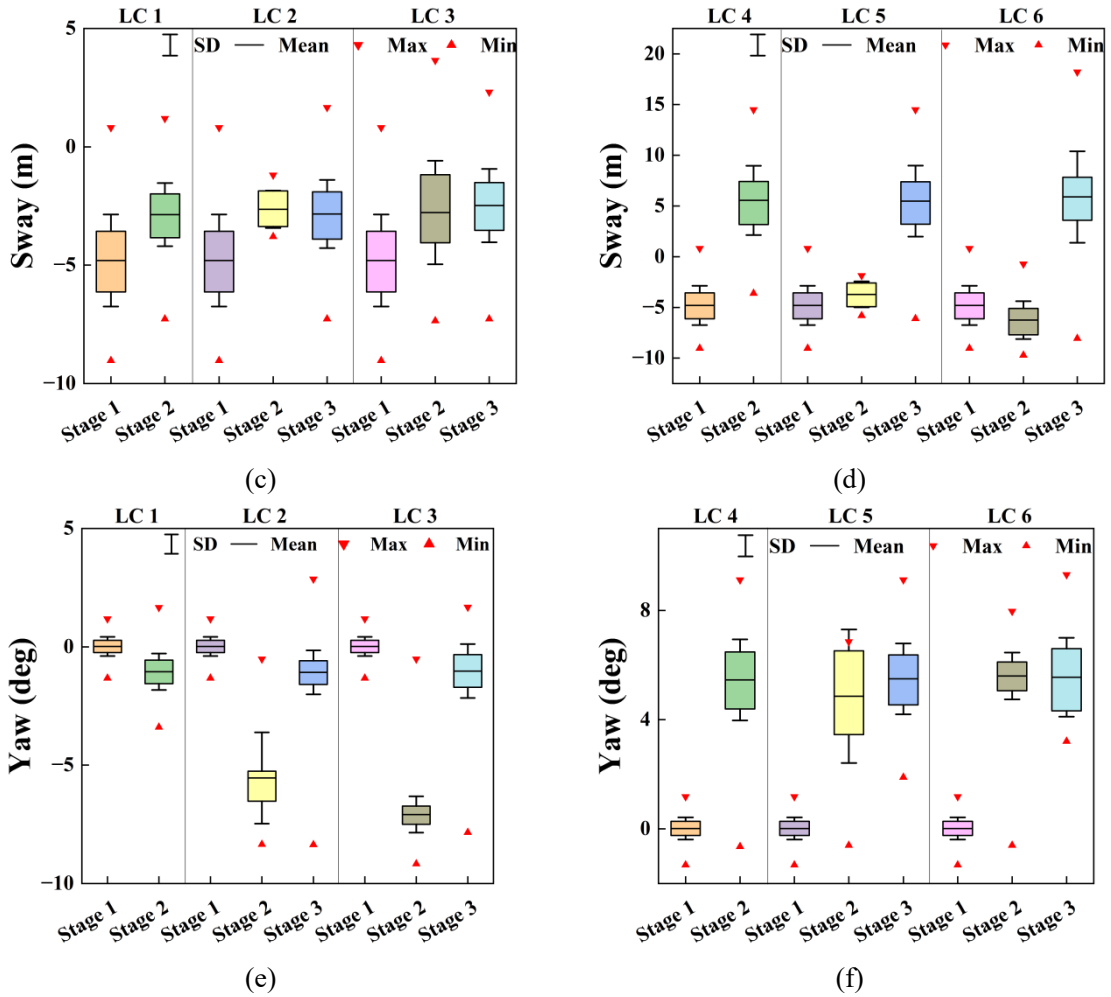


Fig. 10 Statistics for motion responses in rated sea conditions

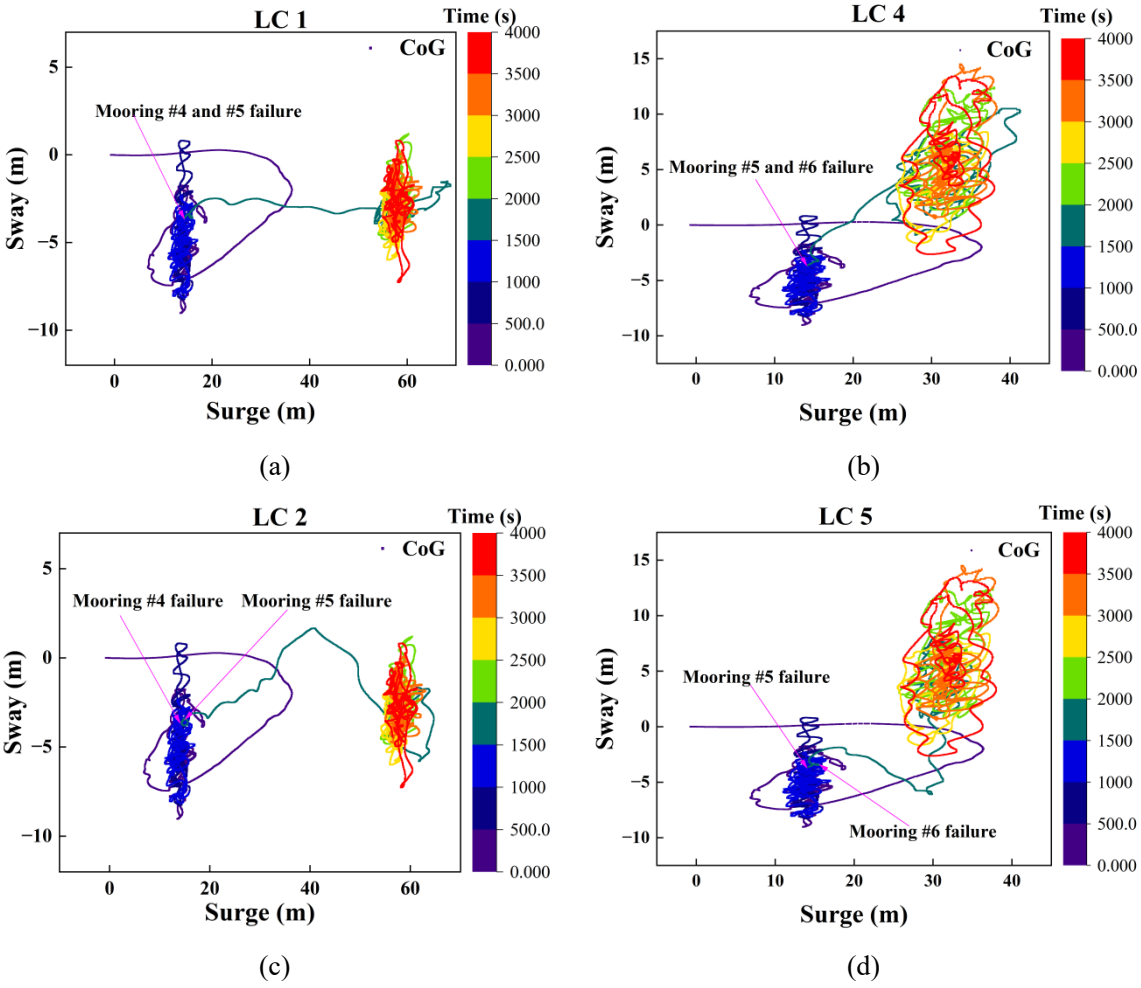
Fig. 10 illustrates the maximum, minimum, average, and standard deviation values during the three stages. Fig. 10(a), (c), and (e) display the statistical indicators of surge, sway, and yaw of the platform after the failure of mooring lines #4 and #5, respectively. Fig. 10(b), (d), and (f) show the statistical indicators of surge, sway, and yaw of the platform after the failure of mooring lines #5 and #6, respectively. It is important to note that LC 1 and LC 4 consist of only two stages.

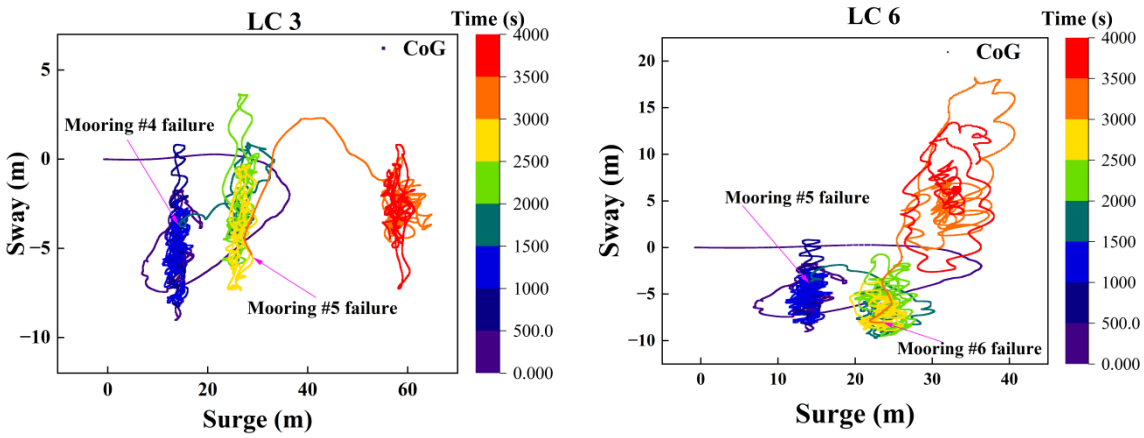
Examining Fig. 10(a) and (b), the average values for the three stages in LC 3 are 14.3m, 26.52m, and 57.16m, while for LC 6, they are 14.3m, 23.78m, and 31.93m. In the surge direction, the average values gradually increase with the failure of mooring lines #4 and #5, indicating a significant increase in surge motion after their failure. Additionally, as the time interval between the failure of two mooring lines increases, the maximum value of surge decreases. This suggests that a shorter interval leads to a less stable wind turbine.

In Fig. 10(c) and (d), the average sway values in the intact mooring state were recorded as -4.81m. However, following the failure of two mooring lines, LC 1, LC 2, and LC 3 exhibited average sway values of -2.87m, -2.84m, and -2.48m, respectively, accompanied by standard deviations of 1.34m, 1.44m, and 1.55m. Conversely, in LC 4, LC 5, and LC 6, the average sway values reached 5.55m, 5.49m, and 5.38m, with corresponding standard deviations of 3.41m, 3.5m, and 4.5m.The observed trend reveals that the sway amplitude decreases and shifts towards the negative range upon the failure of mooring lines #4 and #5. In contrast, when mooring lines #5 and #6 fail, the sway amplitude of the platform exhibits a positive range, with standard deviations that are 2.54, 2.43, and

2.9 times higher than the former case. These findings indicate that the wind turbine becomes even more unstable when two mooring lines in the same corner experience failure.

Yaw plays a significant role in the platform's sway motion, as it influences the lateral aerodynamic force acting on the wind turbine. Changes in the yaw deviation angle lead to variations in the lateral force, subsequently initiating sway motion. Fig. 10(c) and (e) illustrate that a negative yaw angle corresponds to negative sway values, while Fig. 10(d) and (f) demonstrate that a positive yaw angle corresponds to positive sway values. This establishes the clear relationship between sway and yaw. Upon further examination of Fig. 10(e), it is evident that when the failure is limited to mooring #4, the average pitch angle registers at -5.92°. However, in the event of simultaneous failure of both moorings, the average pitch angle notably diminishes to -1.08°. This observation serves to substantiate the notion that in the prevailing sea conditions, the failure of a solitary mooring precipitates a substantial augmentation in the platform's yaw angle.





(e) (f)

Fig. 11 Platform motion trajectory of CoG in rated sea conditions

Fig. 11(a), (c), and (e) present the trajectory of the platform's center of gravity on the sea surface following the failure of mooring lines #4 and #5. Similarly, Fig. 11(b), (d), and (f) display the trajectory of the center of gravity and its projection after the failure of mooring lines #5 and #6.

From the projection graphs, it is evident that the wind turbine initially drifts in the positive X-axis direction due to wind and wave loads and then returns towards its equilibrium position under the influence of the mooring lines. A comparison between the projection graphs in Fig. 11(a) and (c) reveals a distinct curve in the trajectory on the sea surface in Fig. 11(c) when there is a 60s interval between the failures of mooring lines #4 and #5. This curve arises from the sequential failure of mooring lines #4 and #5, which leads to a symmetrical arrangement of the remaining mooring lines along the X-axis. As a result, the uneven distribution of forces on the platform is reduced, causing transverse drift. A similar scenario is observed in Fig. 11(e). It can be observed that after the failures of mooring lines #5 and #6, the wind turbine exhibits a larger drift range, making it more prone to collisions and cable ruptures. Therefore, the failure of mooring lines in the same corner can potentially lead to more severe consequences.

3.2.2 The variation of mooring line tension

The tension in the mooring lines is a crucial indicator of the safety status of the mooring system. The buoyancy effect leads to variations in tension among different nodes, with the highest tension typically observed at the fairlead. When a mooring line fails, the remaining mooring lines experience a redistribution of tension, with the most significant increase occurring in the adjacent mooring lines. This redistribution of tension can amplify the potential risks associated with the failure.

To simulate the effect of mooring line failure, the tension in the failed line is set to 0. This allows for the calculation of the tension in the remaining mooring lines under rated sea conditions. Statistical analysis is then performed on the characteristic values at different stages to investigate the factors contributing to variations in mooring line tension.

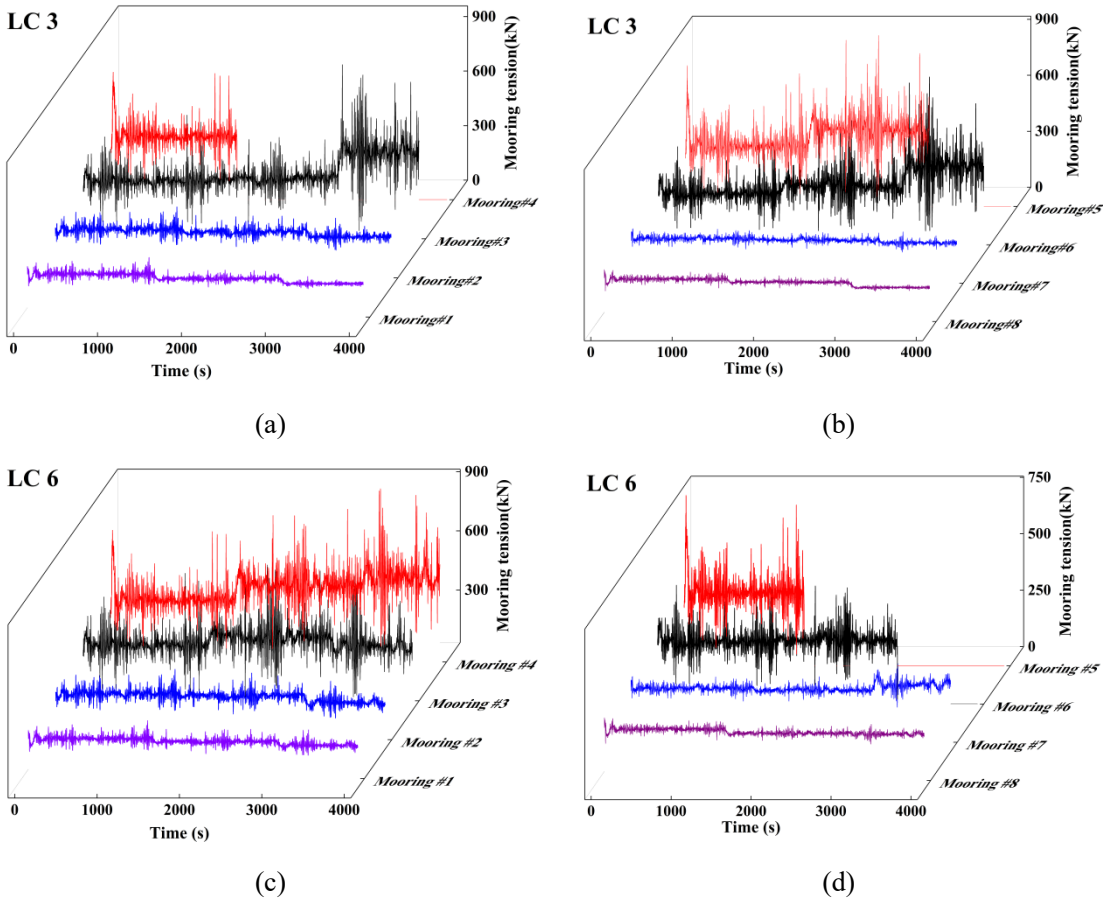


Fig. 12 Comparison of mooring tension between LC3 and LC 6 in rated sea conditions

For the purpose of comparing the changes in remaining mooring line tensions after the failure of one or two mooring lines, Fig. 12 visually presents the tension variations under rated sea conditions with a time interval of 1500s between the line failures. In Fig. 12(a) at 1500s, the failure of mooring line #4 results in a rapid increase in tension in the adjacent mooring lines #3 and #5. This increased tension is a result of the redistribution of forces within the mooring system. Moving to Fig. 12(b) at 3000s, the failure of mooring line #5 leads to a significant increase in tension, particularly in mooring line #6, which is located in the same corner as the failed line. This observation highlights the influence of localized failures on the tension distribution in the adjacent mooring lines. Conversely, the tension in the downwind mooring lines #1, #2, #7, and #8 decreases. This discrepancy can be attributed to the fact that the tension in the downwind mooring lines is primarily influenced by their own weight and is less responsive to environmental loads. As the wind turbine drifts downwind, the length of the mooring line lying on the seabed increases, resulting in a decrease in tension.

In Fig. 12 (d), when mooring line #5 fails at 1500s, the tension variation in the upwind mooring line #4 is the most significant. At 3000s, when mooring line #6 fails, the tension in mooring line #4 continues to increase. Despite mooring line #7 being located on the downwind side, its tension also experiences a slight increase due to its adjacency to mooring line #6. Additionally, the tension in mooring line #3 gradually increases as subsequent mooring lines fail.

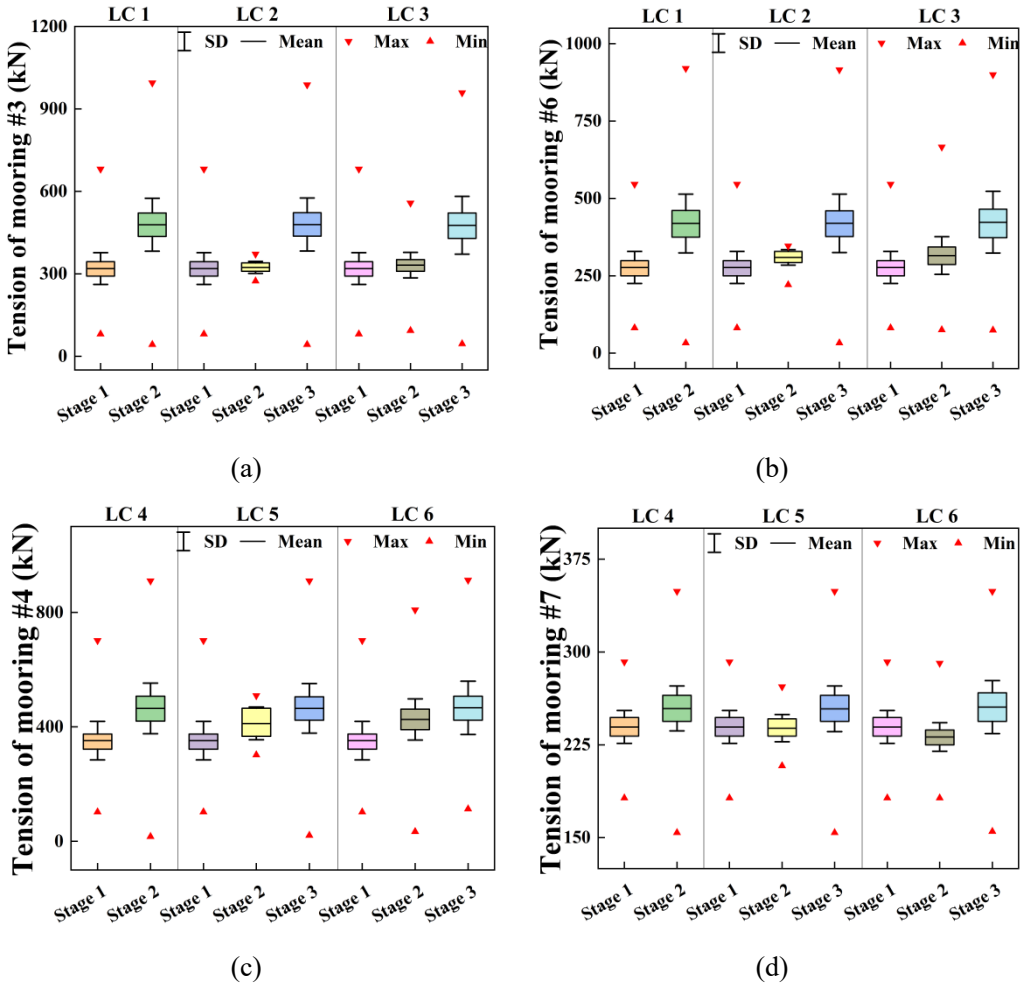


Fig. 13 Statistics for mooring tension in rated sea conditions

The failure of mooring lines leads to notable tension variations in adjacent mooring lines. Fig. 13(a) and (b) depict the characteristic values of tension variations in neighboring mooring lines #3 and #6 following the failure of mooring lines #4 and #5, respectively. Correspondingly, Fig. 13(c) and (d) illustrate the characteristic values of tension variations in neighboring mooring lines #4 and #7 subsequent to the failure of mooring lines #5 and #6. A careful examination of these graphs reveals a discernible pattern: the average tension values in adjacent mooring lines exhibit a gradual increase as mooring lines fail.

For mooring lines #3 and #6, their symmetrical placement about the X-axis leads to similar trends in tension variations. However, when mooring lines #4 and #5 fail, the predominant negative sway of the platform causes the center of gravity to shift away from the anchor point of mooring line #3. As a result, mooring line #3 experiences higher tension compared to mooring line #6. This observation is further supported by empirical data. In LC 3, the average tension in mooring line #3 is recorded as 318.9 kN, 331.5 kN, and 476.7 kN, while for mooring line #6, it is 276.9 kN, 315.4 kN, and 423.1 kN. The standard deviation of tension in mooring line #3 increases from 58.13 kN to 105.13 kN after the failure, almost doubling in magnitude. This indicates a significant rise in tension variation amplitude.

Furthermore, in the case of simultaneous failure of both mooring lines, during the third stage in LC 1, LC 2, and LC 3, the maximum tension observed in mooring line #3 reaches 994.8 kN, 987.5 kN, and 958.8 kN, respectively. In contrast, for mooring line #6, the maximum tension

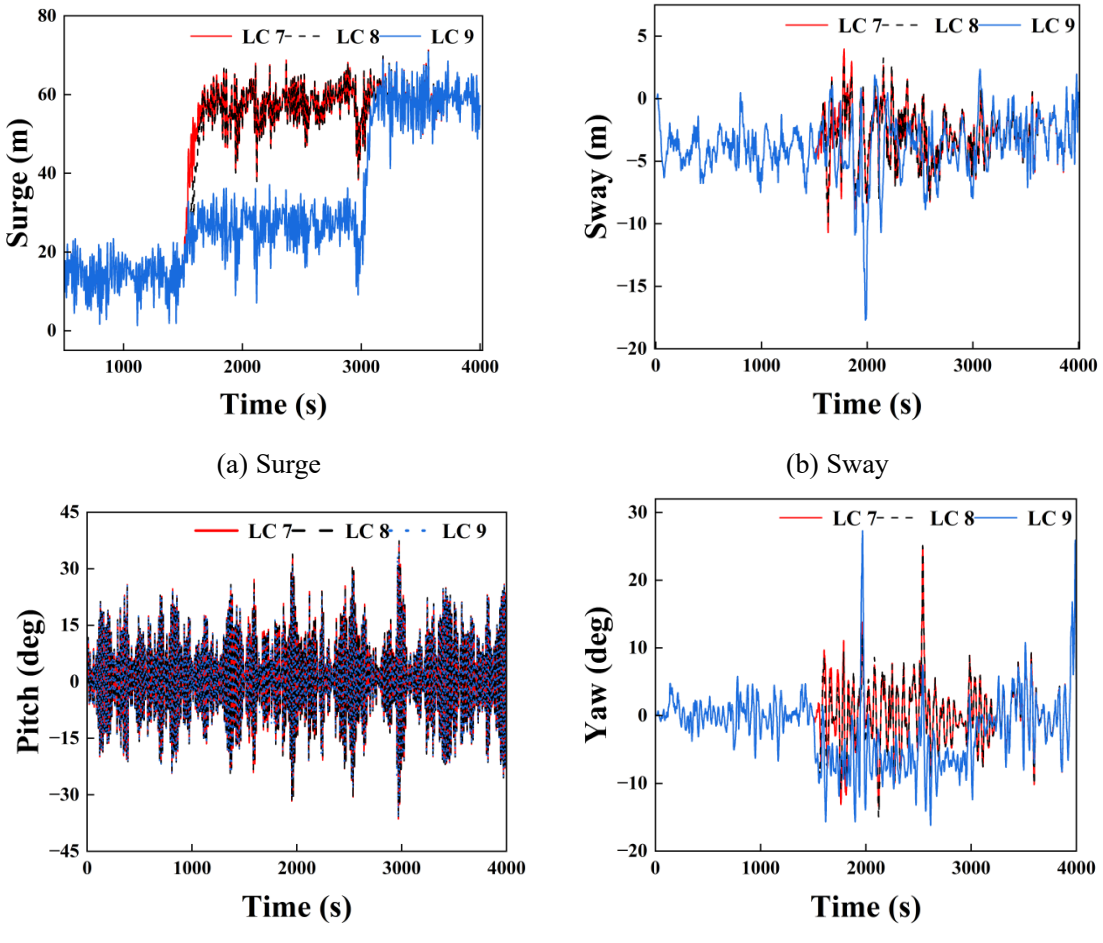
gradually decreases to 920.1 kN, 916.2 kN, and 899.6 kN, respectively. This trend suggests a diminishing tension level in mooring line #3 and #6. Overall, these findings highlight that the simultaneous failure of two mooring lines results in the least stable condition for the wind turbine.

For mooring lines #4 and #7, their respective locations on the upwind and downwind sides play a crucial role in their tension variations. When mooring lines #5 and #6 fail, the platform primarily undergoes a positive roll motion, causing the center of gravity to move away from the anchor point of mooring line #7. Consequently, the tension in mooring line #7 experiences a gradual increase, although this increment is notably smaller compared to the tension variation observed in the upwind mooring line #4. Empirical data confirms this trend, as seen in LC 6, where the average tension in mooring line #4 is recorded as 352 kN, 425.8 kN, and 466.7 kN, while for mooring line #7, it is 239.4 kN, 231.3 kN, and 255.47 kN. These findings align well with the predicted behavior.

3.3 Extreme sea conditions

3.3.1 The dynamic response of the platform

In this section, an analysis of the platform's six degrees of freedom under extreme sea conditions was conducted, and characteristic values for each stage were determined. The computed results provide insights into the dynamic behavior of the wind turbine.



(a) Surge (b) Sway

(c) Heave (d) Yaw

Fig. 14 Dynamic response of the platform after the failure of mooring # 4 and # 5 in extreme sea conditions

Fig. 14 illustrates the platform's motion response following the failure of mooring lines #4 and #5 under extreme sea conditions. In comparison to the nominal sea conditions, the amplitude and frequency of the platform's motion are substantially amplified. The surge displacement surpasses

the sway, which predominantly manifests in the negative region. Using LC 9 as a representative case, the surge motion exhibits three distinct stages, with the platform achieving its maximum drift in the third stage subsequent to the failure of both mooring lines.

At 1500s, with the failure of mooring line #4 while mooring line #5 remains intact, the platform experiences a clockwise rotation driven by the combined influence of wind and wave loads. Due to the alignment of the incident wind with the rotor, the wind turbine undergoes motion in the negative Y-axis direction, resulting in significant sway and yaw changes during the second stage. In extreme sea conditions, when the upwind mooring lines fail, buoyancy forces cause the wind turbine to tilt, increasing the contact area between the platform and the waves. This amplifies the upward force component of the wave loads and enhances the platform's tilt, thereby contributing to increased pitch and roll.

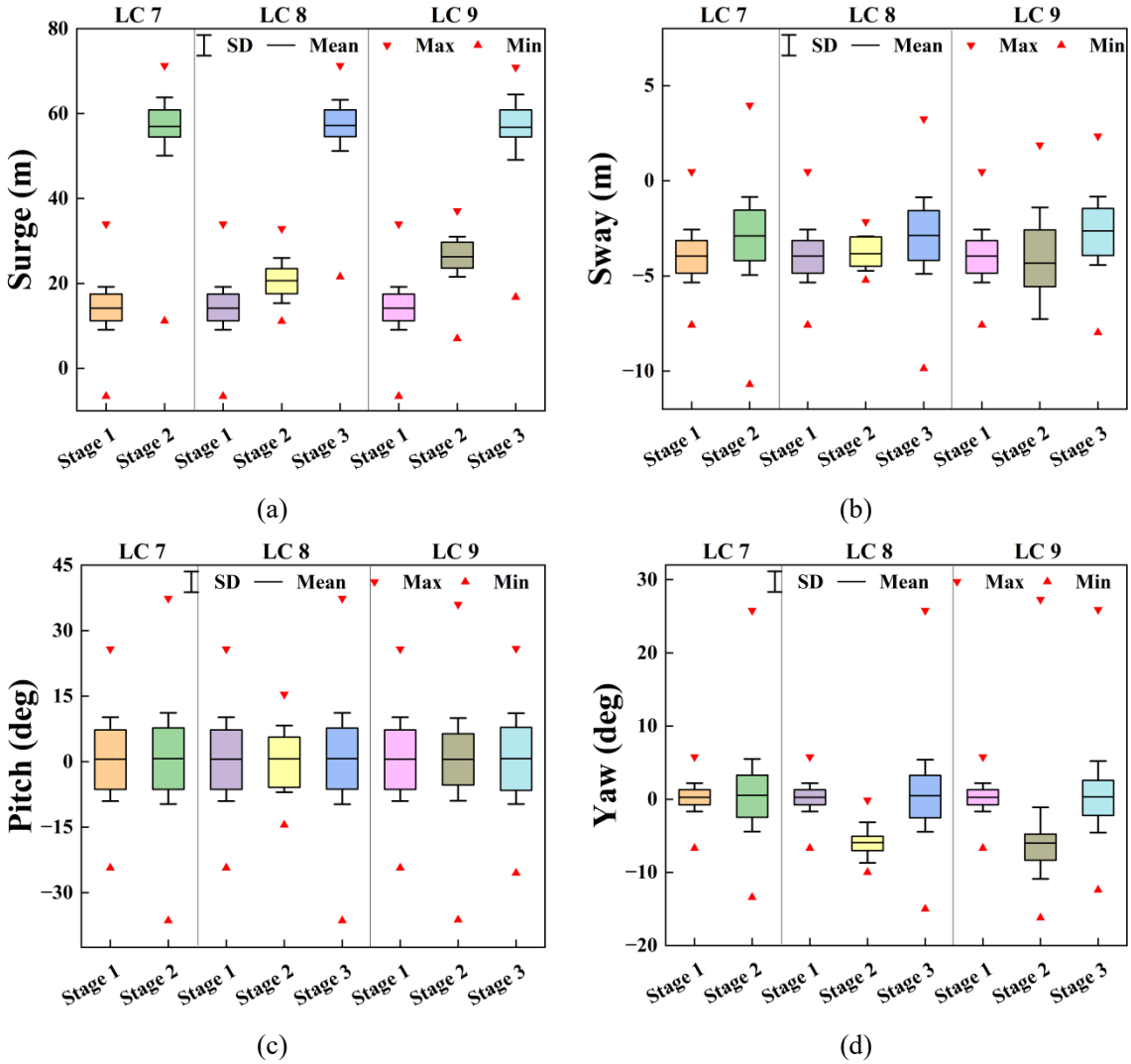


Fig. 15 Statistics for motion responses of the platform after the failure of mooring # 4 and # 5 in extreme sea conditions

Fig. 15 presents the maximum, minimum, mean, and standard deviation values of surge, sway, yaw, and heave for the three stages following the failure of mooring lines #4 and #5 in extreme sea conditions.

In Fig. 15(a), the surge parameter exhibits a gradual increase with the failure of successive mooring lines. In LC 9, the maximum surge values for the three stages are recorded as 34m, 37.14m,

and 70.85m, respectively. Notably, the impact on the platform is relatively minor when a single mooring line fails. However, with the simultaneous failure of both mooring lines, the maximum drift distance of the platform doubles compared to the previous stages.

Fig. 15(b) and (d) represent the sway and yaw parameters, respectively, with both exhibiting negative mean values. In LC 9, the minimum sway values for the second and third stages are recorded as -17.7m and -7.9m, respectively, while the minimum yaw values are -16.2°and -12.4°, respectively, with the second stage exhibiting a larger magnitude. These findings indicate that the failure of a single mooring line has a substantial impact on the platform's sway and yaw. As mooring lines #4 and #5 are positioned on the upwind side, their failure results in significant inclination of the wind turbine when subjected to extreme wind and wave loads. Consequently, there is a notable increase in platform pitch. In LC 9 of Fig. 15(c), the maximum value and standard deviation of pitch are recorded as 36.04°and 9.48°, respectively, which are approximately 3.9 times and 3.3 times larger compared to the nominal sea conditions. These results highlight the substantial increase in both the amplitude and frequency of the platform's motion under extreme sea conditions.

3.3.2 The variation of mooring line tension

In this section, we calculate the tensions of the remaining mooring lines after the failure of mooring lines #4 and #5 under extreme sea conditions. We then conduct a statistical analysis of the characteristic values in the three stages to investigate the factors contributing to the changes in mooring tension.

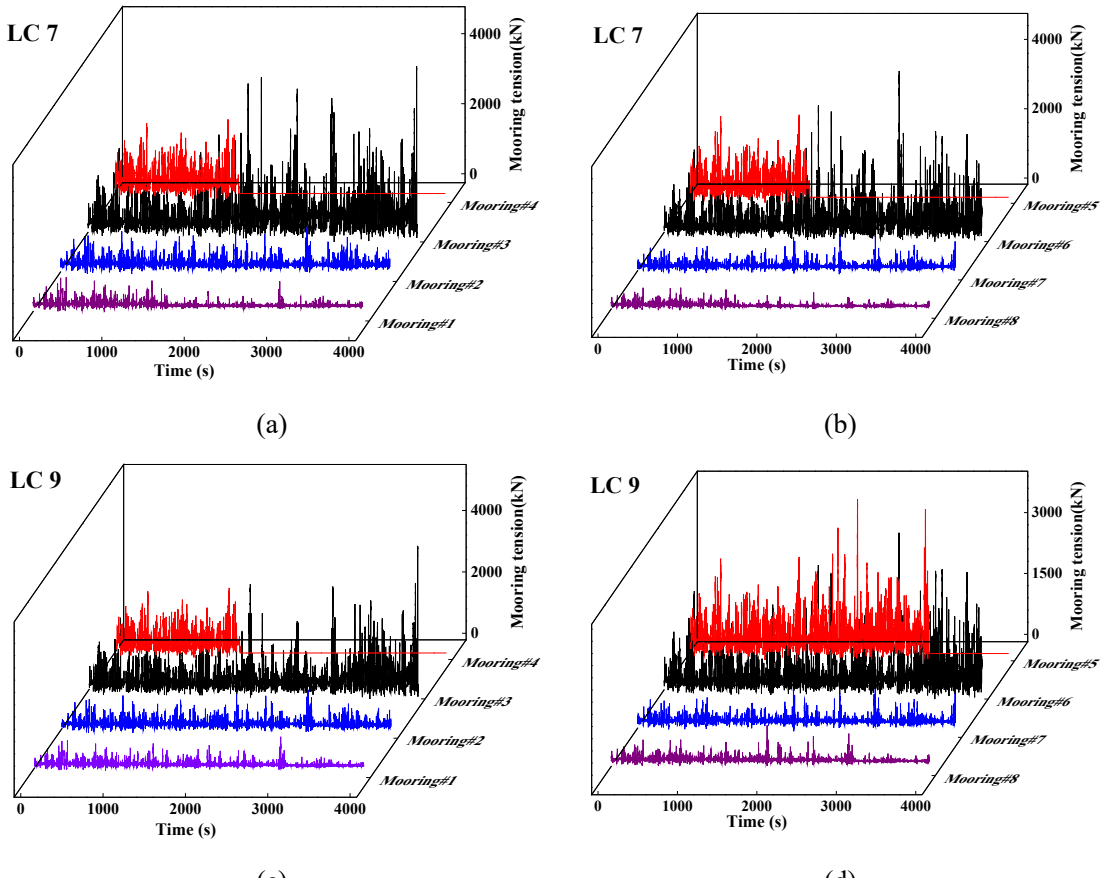
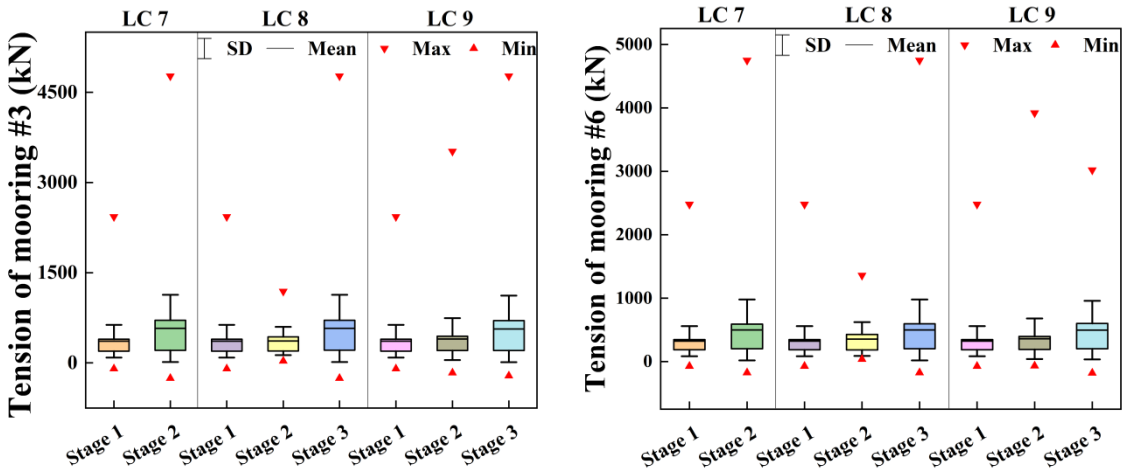


Fig. 16 Comparison of mooring tension in extreme sea conditions of LC 7 and LC 9

Fig. 16 depicts the tension variations of the eight mooring lines under extreme sea conditions, specifically focusing on the simultaneous failure of mooring lines #4 and #5, as well as their

subsequent sequential failures with a time interval of 1500s. These tension variations are significantly intensified compared to the rated sea conditions. Interestingly, even the mooring lines on the downwind side, such as #2 and #7, exhibit an increasing trend in tension. Meanwhile, the tension of the upwind mooring lines experiences a notable increase, particularly mooring lines #3 and #6, which approach the load limit. This observed phenomenon can be attributed to the influence of the distance between the fairlead and the anchor points on mooring tension. The dynamic response of the platform undergoes a sharp increase, leading to drastic fluctuations and variations in mooring tension. Consequently, compared to the rated sea conditions, the mooring system becomes more vulnerable to damage, highlighting the need for stricter design and installation requirements to ensure stability and safety. Moreover, when comparing LC 7 and LC 9, it can be observed that the tension increment for mooring lines #3 and #6 is slower when they fail sequentially with a time interval of 1500s.



(a) (b)

Fig. 17 Statistics for mooring tension in extreme sea conditions

Fig. 17(a) and (b) showcase the statistical values of tension variations in the neighboring mooring lines #3 and #6 following the failure of mooring lines #4 and #5. Examining mooring line #3 as an example, the standard deviations for the second stage of LC 7, LC 8, and LC 9 are observed to be 5.8, 10.8, and 7.48 times higher, respectively, compared to the values under rated sea conditions. This highlights that the oscillation amplitude of mooring tension under extreme sea conditions is significantly amplified compared to rated sea conditions. In LC 9, the average tensions of mooring line #3 during the three stages are recorded as 360.64 kN, 397.14 kN, and 566.06 kN, respectively. Similarly, for mooring line #6, the average tensions during the three stages are 321.53 kN, 361.54 kN, and 496.57 kN, respectively. It is worth noting that mooring line #3 exhibits higher average tension due to the counterclockwise rotation of the platform inducing a negative direction of sway motion, resulting in greater elongation of mooring line #3. Notably, the maximum tension recorded in mooring line #3 reaches 4771 kN, which represents approximately 66.3% of the ultimate breaking strength.

3.3.3 Effects of the shutdown measure

In extreme sea conditions, it is a standard procedure to shut down the wind turbine in order to prioritize safety and mitigate potential risks. This proactive measure helps prevent equipment overload, mooring failure, and any further damage that could occur. By shutting down the wind turbine, the aim is to ensure the long-term reliability and sustainability of the system for power

generation while safeguarding the overall integrity of the mooring system and the wind turbine components.

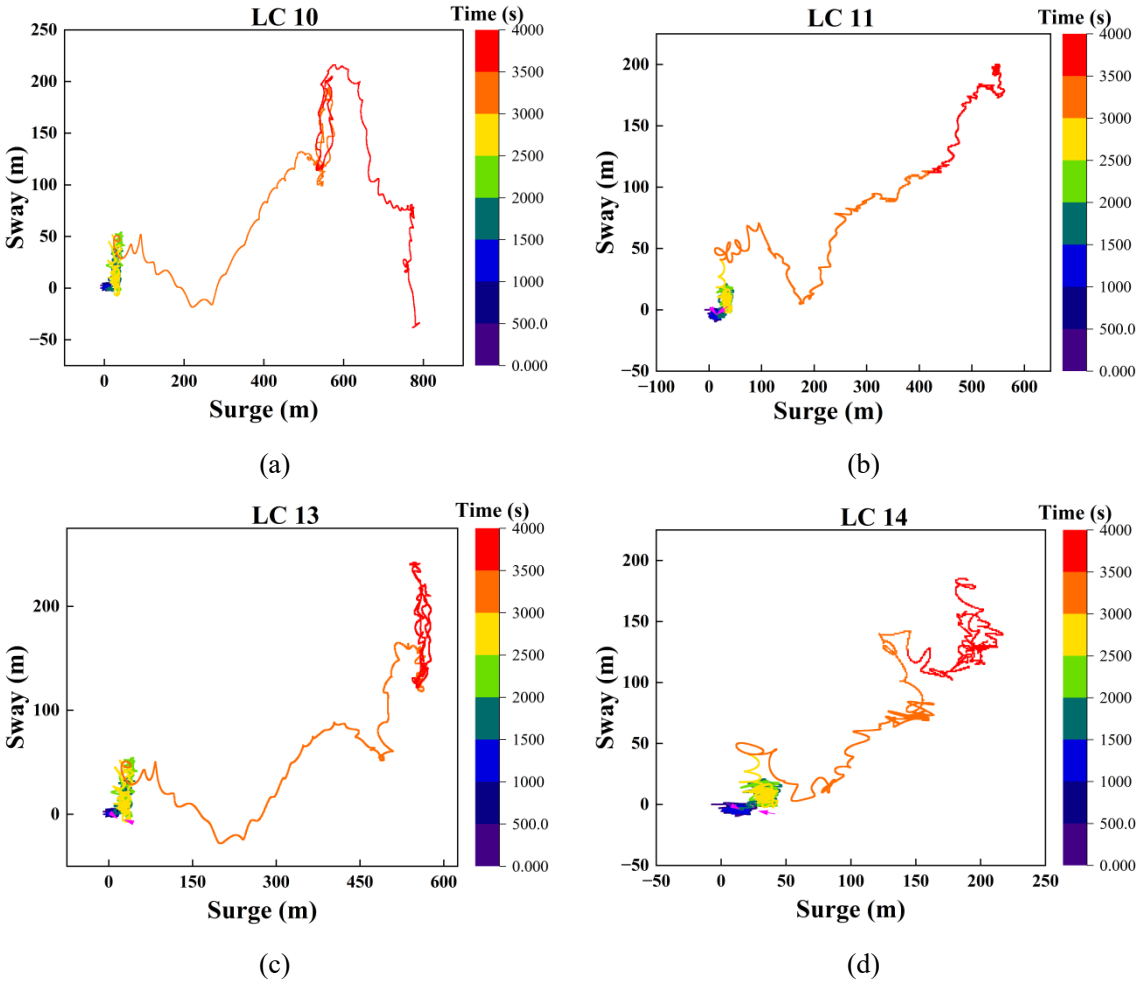


Fig. 18 Platform motions trajectory after the failure of mooring # 5 and # 6 in extreme sea conditions

In Fig. 18(a) and (b), the trajectories of the platform's center of gravity are depicted following the successive failures of mooring #5 and #6 with intervals of 0s and 60s, respectively. Fig. 18(c) and (d) illustrate the platform's trajectory after the wind turbine is deactivated under the same LC 10 and LC 11 conditions. It is evident that the platform has lost control.

Prior to wind turbine deactivation, LC 10 and LC 11 exhibit maximum surge displacements of 790.3m and 561.7m, respectively. After implementing pitch control, LC 13 and LC 14 demonstrate reduced maximum surge displacements of 576.8m and 216.7m, respectively. This signifies a noteworthy decrease in aerodynamic loads resulting from the shutdown measures, leading to a significant reduction in platform surge. However, it is important to note that the platform's drift distance still exceeds the range observed under normal sea conditions. This behavior can be attributed to the shallow draft and relatively high overall center of gravity of the Barge platform, rendering it susceptible to wind and wave excitations and prone to deviation in motion. Consequently, it is deemed unsuitable for deployment in harsh offshore environments.

Furthermore, in LC 12 with a time interval of 1500s, the simulation results demonstrate that there were no successive mooring failures. This observation indicates that a shorter interval between mooring failures leads to a less stable wind turbine. Additionally, when comparing LC 7 and LC 8 that are also extreme sea conditions, it can be observed that the platform remains under control after

the failure of moorings #4 and #5, which are located on the same side of the platform. This suggests that the more concentrated the mooring failures are, the more severe the platform's dynamic response becomes.

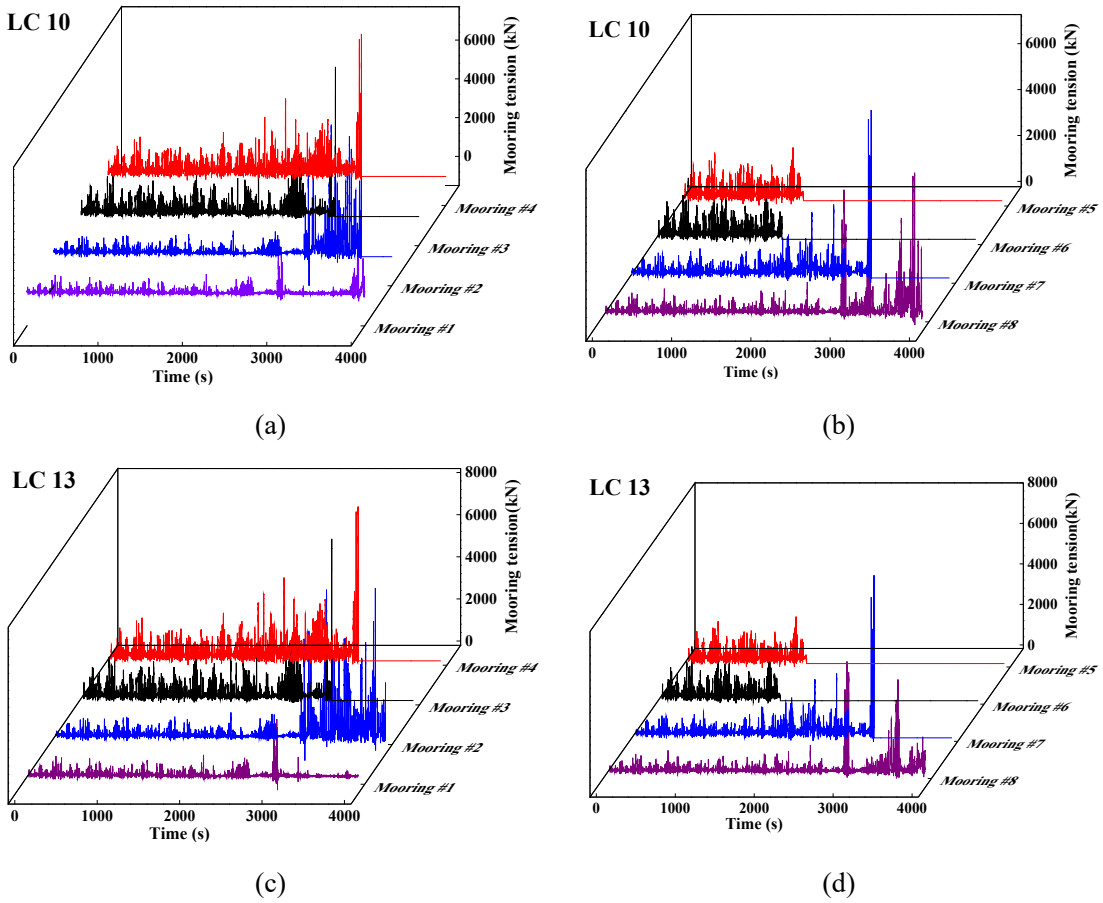


Fig. 19 Comparison of the mooring tensions between the LC 10 and LC 13 before and after wind turbine shutdown

In Fig. 19, the tension variations of the eight moorings before and after shutting down the wind turbine are depicted after the simultaneous failures of moorings #5 and #6 under extreme sea conditions. At 4000s in LC 10, six moorings have already experienced successive failures, while mooring #8 has not failed yet but undergoes a maximum tension of 6265.7kN. Using formula (1), the safety factor of mooring #8 is calculated to be 1.15. After the wind turbine is shut down, in LC13, five moorings still fail, and the safety factor of mooring #2 is calculated to be 1.03, which is below the required value of 1.05 as per the specifications. Consequently, it fails to meet the redundancy requirement of the mooring system and is prone to rapid failure. Even if the remaining two moorings remain intact, they are unable to maintain the wind turbine's stability in such harsh environmental conditions.

When the mooring system is functioning normally, the structure of the floating wind turbine is at its most stable and capable of withstanding environmental loads. However, over time, fatigue wear affects the mooring system, resulting in the reserve tension value being significantly lower than the design requirement. Under extreme sea conditions, once a mooring fails, the sudden and intense impact induces a rapid increase in tension in the remaining moorings, triggering a progressive failure process.

4. Conclusions

This article employs a coupled method of FAST and AQWA to analyze and compare the dynamic responses of the wind turbine platform and the variations in remaining mooring tensions when two mooring lines fail in the same corner of the platform and when two mooring lines fail on the same side. The following conclusions have been drawn:

(1) In rated sea conditions, the failure of mooring lines #4 and #5 results in increased surge distance, while the failure of #5 and #6 leads to greater sway distance. There is a notable correlation between sway and yaw movements, with yaw playing a significant role in the magnitude of sway. This further underscores the pronounced influence of mooring line #6 failure on sway motion and highlights that mooring line #5 has a more substantial impact on yaw motion.

(2) In rated sea conditions, after the first mooring failure, the platform reaches its maximum surge distance from the original position in 61.7s. Concurrent failure of two moorings results in the highest drift speed of the platform, causing increased wind turbine instability. When the mooring failures occur 60s apart, the disturbances accumulate, prolonging the stabilization time of the platform. A 1500s interval between the mooring failures leads to the least amplitude change. Additionally, the failure of mooring lines causes significant tension variations in the adjacent mooring lines.

(3) In extreme sea conditions, the maximum value and standard deviation of pitch are 36.04° and 9.48°, about 3.9 and 3.3 times larger than in rated sea conditions. When mooring lines #4 and #5 fail, the platform still achieves a new equilibrium. After the failure of a single mooring line, the platform is most affected in terms of sway and yaw motion, while the failure of two mooring lines markedly increases surge motion, up to 2.08 times the original value.

(4) Following the failure of two adjacent mooring lines, tensions in neighboring mooring lines increase significantly. Mooring line #3 experiences a maximum tension of 4771 kN, which is 1.57 times higher than before the failure and reaches 66.3% of its breaking limit. Meanwhile, the maximum tension in mooring line #6 is slightly less than that in mooring line #3.

(5) When mooring lines #5 and #6 fail together or within a 60s interval, it triggers a progressive failure in the mooring system. However, a 1500s interval between failures allows the wind turbine platform to stabilize. This indicates that concentrated mooring lines failure and shorter interval lead to more severe platform responses. After the wind turbine shutdown, five moorings still experience failure, and the safety factor of mooring #2 dropping to 1.03, below the specified requirement of 1.05. This sensitivity to wind and wave excitations makes the barge platform unsuitable for harsh sea conditions.

These results highlight the dynamic behavior of the platform under various mooring line failure scenarios, offering key insights for wind turbine design and operation. This is particularly important for assessing the feasibility of FOWT system in harsh marine environments. These findings provide valuable guidance for future engineering designs and operational strategies, aiming to enhance the safety and reliability of such system in challenging conditions.

Acknowledgements

The authors would like to acknowledge the support of National Natural Science Foundation of China (Grand No. 52006148, 52101317, 52106262 and 52376204), and the support of the non-carbon energy conversion and utilization institute under the Shanghai Class IV Peak Disciplinary Development Program.

References

[1] Soares P M M, Lima D C A, Nogueira M. Global offshore wind energy resources using the new ERA-5 reanalysis. Environmental Research Letters, 2020, 15(10): 1040a2.

[2] Council G W E. Global wind report 2022. 2022. URL https://gwec. net/global-wind-report-2022/,(Accessed: 2022-08-17).

[3] Xiaohui L I U, Renjie G A O, Yu X U E. Current situation and future development trend of floating offshore wind turbine. Distributed Energy Resources, 2020, 5(3): 39-46.

[4] Strivens, S.; Northridge, E.; Evans, H.; Harvey, M.; Camp, T.; Terry, N. Floating Wind Joint Industry Project Phase III Summary Report; The Carbon Trust: London, UK, 2021.

[5] Arias R R, Ruiz Á R, de Lena Alonso V G. Mooring and anchoring. Floating Offshore Wind Farms, 2016: 89-119.

[6] Technology, S.S. Advanced Anchoring and Mooring Study; Oregon Wave Energy Trust (OWET): Portland, OR, USA, 2009.

[7] Altuzarra J, Herrera A, Matías O, et al. Mooring System Transport and Installation Logistics for a Floating Offshore Wind Farm in Lannion, France. Journal of Marine Science and Engineering, 2022, 10(10): 1354.

[8] Lefebvre S. and Collu M., 2012. Preliminary design of a floating support structure for 5 MW offshore wind turbine. Ocean Engineering, vol. 40, pp. 15-26.

[9] Kallesœ, B., Hansen, A., 2011. Dynamic mooring line modeling in hydro-aero-elastic wind turbine simulations. In: Proceedings of the 21st International Offshore and Polar Engineering Conference, ISOPE.

[10] Hall, M., Buckham, B., Crawford, C., 2014. Evaluating the importance of mooring line model fidelity in floating offshore wind turbine simulations. Wind Energy, 1835–1853.

[11] Azcona J, Palacio D, Munduate X, et al. Impact of mooring lines dynamics on the fatigue and ultimate loads of three offshore floating wind turbines computed with IEC 61400-3 guideline. Wind Energy, 2017, 20(5): 797-813.

[12] Ansys A. AQWA theory manual. AQWA: Canonsburg, PA, USA, 2013.

[13] Masciola M, Robertson A, Jonkman J, et al. Assessment of the importance of mooring dynamics on the global response of the DeepCwind floating semi-submersible offshore wind turbine//The Twenty-third International Offshore and Polar Engineering Conference. OnePetro, 2013.

[14] Masciola M, Robertson A, Jonkman J, et al. Investigation of a FAST-OrcaFlex coupling module for integrating turbine and mooring dynamics of offshore floating wind turbines. National Renewable Energy Lab.(NREL), Golden, CO (United States), 2011.

[15] Wendt F F, Andersen M T, Robertson A N, et al. Verification and validation of the new dynamic mooring modules available in FAST v8//The 26th International Ocean and Polar Engineering Conference. OnePetro, 2016.

[16] Jonkman J M. Dynamics modeling and loads analysis of an offshore floating wind turbine. University of Colorado at Boulder, 2007.

[17] Matha D, Hauptmann S, Hecquet T, et al. Methodology and results of loads analysis of wind turbines with advanced aeroelastic multi-body simulation. DEWEK, Bremen, 2010.

[18] Jassmann U, Berroth J, Matzke D, et al. Model predictive control of a wind turbine modeled in Simpack//Journal of Physics: Conference Series. IOP Publishing, 2014, 524(1): 012047.

[19] Armendáriz J A, Echarri X M, Nygaard T A, et al. Development of OPASS code for dynamic simulation of mooring lines in contact with seabed. EWEA offshore 2011 proceedings, 2011.

[20] Robertson, A., Jonkman, J., Masciola, M., Song, H., Goupee, A., Coulling, A., Luan, C.,2014. Definition of the Semi-submersible Floating System for Phase II of OC4.Technical Report TP-5000-60601 NREL.

[21] Yang Y, Bashir M, Michailides C, et al. Development and application of an aero-hydro-servo-elastic coupling framework for analysis of floating offshore wind turbines. Renewable Energy, 2020, 161: 606-625.

[22] Collu M, Borg M. Design of floating offshore wind turbines//Offshore wind farms. Woodhead Publishing, 2016: 359-385.

[23] Zhang H, Wang H, Cai X, et al. Novel method for designing and optimising the floating platforms of offshore

wind turbines. Ocean Engineering, 2022, 266: 112781.
[24] Li Y, Zhu Q, Liu L, et al. Transient response of a SPAR-type floating offshore wind turbine with fractured mooring lines. Renewable Energy, 2018, 122: 576-588.
[25] Wu H, Zhao Y, He Y, et al. Transient response of a TLP-type floating offshore wind turbine under tendon failure conditions. Ocean Engineering, 2021, 220: 108486.
[26] Ren Y, Venugopal V, Shi W. Dynamic analysis of a multi-column TLP floating offshore wind turbine with tendon failure scenarios. Ocean Engineering, 2022, 245: 110472.
[27] Yang Y, Bashir M, Li C, et al. Investigation on mooring breakage effects of a 5 MW barge-type floating offshore wind turbine using F2A. Ocean Engineering, 2021, 233: 108887.
[28] Bae Y H, Kim M H, Kim H C. Performance changes of a floating offshore wind turbine with broken mooring line[J]. Renewable Energy, 2017, 101: 364-375.
[29] Yang R Y, Chuang T C, Zhao C, et al. Dynamic response of an offshore floating wind turbine at accidental limit states—mooring failure event. Applied Sciences, 2022, 12(3): 1525.
[30] Subbulakshmi A, Verma M. Transient response reduction of floating offshore wind turbine subjected to sudden mooring line failure. Ocean Engineering, 2023, 271: 113702.
[31] Tang H J, Yao H C, Yang R Y. Experimental and numerical study of a barge-type floating offshore wind turbine under a mooring line failure. Ocean Engineering, 2023, 278: 114411.
[32] Neisi A, Ghassemi H, Iranmanesh M. Effect of the multi-segment mooring system failure on the dynamic motions of the floating platform. Ocean Engineering, 2023, 290: 116371.
[33] Mansour A M, Gordon B J, Ling Q, et al. TLP survivability against progressive failure of tendon and foundation systems in offshore Western Australian harsh environment//International Conference on Offshore Mechanics and Arctic Engineering. American Society of Mechanical Engineers, 2013, 55317: V001T01A079.
[34] Ahmed M O, Yenduri A, Kurian V J. Evaluation of the dynamic responses of truss spar platforms for various mooring configurations with damaged lines. Ocean Engineering, 2016, 123: 411-421.
[35] Yu J, Hao S, Yu Y, et al. Mooring analysis for a whole TLP with TTRs under tendon one-time failure and progressive failure. Ocean Engineering, 2019, 182: 360-385.
[36] Wayman E N. Coupled Dynamics and Economic Analysis of Floating Wind Turbine Systems. Boston: Massachusetts Institute of Technology, 2006.
[37] Jonkman, J.M., Matha, D., 2011. Dynamics of offshore floating wind turbines—analysis of three concepts. Wind Energy 14 (4), 557–569.
[38] Zhang Z, Wang X, Zhang X, et al. Dynamic responses and mooring line failure analysis of the fully submersible platform for floating wind turbine under typhoon. Engineering Structures, 2024, 301: 117334.
[39] Chuang T C, Yang W H, Yang R Y. Experimental and numerical study of a barge-type FOWT platform under wind and wave load. Ocean Engineering, 2021, 230: 109015.
[40] Liu Q, Miao W, Yue M, et al. Dynamic response of offshore wind turbine on 3× 3 barge array floating platform under extreme sea conditions. China Ocean Engineering, 2021, 35(2): 186-200.
[41] Kopperstad K M, Kumar R, Shoele K. Aerodynamic characterization of barge and spar type floating offshore wind turbines at different sea states. Wind Energy, 2020, 23(11): 2087-2112.
[42] Aboutalebi, P.; M'zoughi, F.; Garrido, I.; Garrido, A.J. Performance Analysis on the Use of Oscillating Water Column in Barge-Based Floating Offshore Wind Turbines. Mathematics 2021, 9, 475.
[43] Portella R B. Mooring system: From initial design to offshore installation//Offshore Technology Conference. OTC, 2000: OTC-12174-MS.
[44] Jonkman J, Butterfield S, Musial W, et al. Definition of a 5-MW reference wind turbine for offshore system development. National Renewable Energy Lab.(NREL), Golden, CO (United States), 2009.
[45] Qi Y, Shi P. Calculation of the Extreme Wind, Wave And Current In Deep Water of the South China Sea//Third ISOPE International Deep-Ocean Technology Symposium. OnePetro, 2009.
[46] Pierson Jr W J, Moskowitz L. A proposed spectral form for fully developed wind seas based on the similarity theory of SA Kitaigorodskii. Journal of geophysical research, 1964, 69(24): 5181-5190.
[47] Madsen P H, Risø D. Introduction to the IEC 61400-1 standard. Risø National Laboratory, Technical University

of Denmark, 2008.
[48] Jonkman B J. TurbSim user's guide. National Renewable Energy Lab.(NREL), Golden, CO (United States), 2006.
[49] IEC. IEC 61400-3 Ed. 1.0 Wind turbines—design requirements for offshore wind turbines, 2009.
[50] DNV G L. DNV-OS-J101–Design of offshore wind turbine structures. DNV GL, 2014.
[51] ABS A. Guide for Building and Classing Floating Offshore Wind Turbine Installations. The American Bureau of Shipping, Houston (TX), USA, 2013.
[52] Kyokai N K. Guidelines for offshore floating wind turbine structures. Class NK, 2012, 59.
[53] Ansys A. AQWA user’s manual release 17.0. ANSYS Inc.: Canonsburg, PA, USA, 2016.
[54] Jonkman J M, Buhl M L. FAST user's guide. Golden, CO, USA: National Renewable Energy Laboratory, 2005.
[55] Yang Y, Bashir M, Wang J, et al. Performance evaluation of an integrated floating energy system based on coupled analysis. Energy Conversion and Management, 2020, 223: 113308.
[56] Yang Y, Bashir M, Wang J, et al. Wind-wave coupling effects on the fatigue damage of tendons for a 10 MW multi-body floating wind turbine. Ocean Engineering, 2020, 217: 107909.
[57] Ogilvie T F. Second-order hydrodynamic effects on ocean platforms//Proceedings of the international workshop on ship and platform motions, Berkeley. 1983: 205-265.
[58] York M A, Moore G D. Second order hydrodynamic coefficients from kinetic theory. Physical Review D, 2009, 79(5): 054011.